EFFECTS OF TEMPERATURE AND ELECTRIC FIELD

ON LOCAL STRUCTURE OF BARIUM TITANATE

SINGLE CRYSTAL STUDIED BY X-RAY

ABSORPTION SPECTROSCOPY

TECHNIQUE

Phanupong Phaktapha

A Thesis Submitted in Partial Fulfillment of the Requirement for the

Degree of Master of Science in Applied Physics

Suranaree University of Technology

Academic Year 2016

ผลของอุณหภูมิและสนามไฟฟ้าต่อโครงสร้างเฉพาะที่ของผลึกเดี่ยว

แบเรียมไททาเนตซึ่งศึกษาโดยเทคนิคสเปกโทรสโกปี

การดูดกลืนรังสีเอกซ์

นายภาณุพงศ์ ภักตะภา

วิทยานิพนธ์นี้เป็นส่วนหนึ่งของการศึกษาตามหลักสูตรปริญญาวิทยาศาสตรมหาบัณฑิต

สาขาวิชาฟิสิกส์ประยุกต์

มหาวิทยาลัยเทคโนโลยีสุรนารี

ปีการศึกษา 2559

EFFECTS OF TEMPERATURE AND ELECTRIC FIELD ON LOCAL STRUCTURE OF BARIUM TITANATE SINGLE CRYSTAL STUDIED BY X-RAY ABSORPTION SPECTROSCOPY TECHNIQUE

Suranaree University of Technology has approved this thesis submitted in partial fulfillment of the requirements for a Master's Degree.

Thesis Examining Committee

_____
(Asst. Prof. Dr. Worawat Meevasana)

Chairperson

_____
(Assoc. Prof. Dr. Rattikorn Yimnirun)

Member (Thesis Advisor)

_____
(Dr. Saroj Rujirawat)

Member

_____
(Assoc. Prof. Dr. Prayoon Songsiriritthigul)

Member

_____
(Dr. Pinit Kidkhunthod)

Member

_____
(Asst. Prof. Dr. Worawat Meevasana)

Dean of Institute of Science

_____
(Prof. Dr. Santi Maensiri)

Vice Rector for Academic Affairs

and Internationalization

ภาณุพงศ์ ภักตะภา : ผลของอุณหภูมิและสนามไฟฟ้าต่อโครงสร้างเฉพาะที่ของผลึกเดี่ยว
แบเรียมไททาเนตซึ่งศึกษาโดยเทคนิคสเปกโทรสโกปีการดูดกลืนรังสีเอ็กซ์ (EFFECTS
OF TEMPERATURE AND ELECTRIC FIELD ON LOCAL STRUCTURE OF
BARIUM TITANATE SINGLE CRYSTAL STUDIED BY X-RAY ABSORPTION
SPECTROSCOPY TECHNIQUE) อาจารย์ที่ปรึกษา : รองศาสตราจารย์ ดร.รัตติกร
ยิ้มนิรัญ, 77 หน้า

วิทยานิพนธ์นี้เกี่ยวกับผลของอุณหภูมิและสนามไฟฟ้าต่อโครงสร้างเฉพาะที่ของผลึกเดี่ยว
แบเรียมไททาเนตซึ่งศึกษาโดยเทคนิคสเปกโทรสโกปีการดูดกลืนรังสีเอ็กซ์ ซึ่งผลึกเดี่ยวแบเรียม
ไททาเนตถูกปลูกขึ้นด้วยวิธีของเรไมการ์ การตรวจสอบผลของอุณหภูมิต่อโครงสร้างเฉพาะถิ่น
ของผลึกเดี่ยวแบเรียมไททาเนตโดยทำให้ร้อนขึ้นจากอุณหภูมิ 50 100 120 130 ไปจนถึงอุณหภูมิ
150 องศาเซลเซียสและการตรวจสอบอิทธิพลของสนามไฟฟ้าที่มีต่อโครงสร้างเฉพาะถิ่นของผลึก
เดี่ยวแบเรียมไททาเนตโดยการเพิ่มสนามไฟฟ้าภายนอกเข้าไปเริ่มจากไม่มีสนามไฟฟ้าไปจนถึง
เกือบสองเท่าของสนามไฟฟ้าบังคับ ผลของการเพิ่มอุณหภูมิพบว่า อุณหภูมิมีผลต่อการ
เปลี่ยนแปลงโครงสร้างจากเตตระโกนอล ไปยัง โครงสร้างแบบคิวบิกเพอร์โรฟสไกป์ นอกจากนั้น
ผลของสนามไฟฟ้าจะทำให้อะตอมไทเทเนียมที่อยู่ในโครงสร้างของแบเรียมไททาเนตเกิดการ
เปลี่ยนตำแหน่งจากตรงกลางของผลึก ซึ่งผลการทดลองดังกล่าวสามารถยืนยันด้วยผลการคำนวณ
จากโปรแกรม FeFF8.2

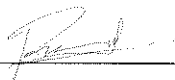|	
สาขาวิชาฟิสิกส์	ลายมือชื่อนักศึกษา_____
ปีการศึกษา 2559	ลายมือชื่ออาจารย์ที่ปรึกษา_____
	ลายมือชื่ออาจารย์ที่ปรึกษาร่วม_____

PHANUPONG PHAKTAPHA : EFFECTS OF TEMPERATURE AND
ELECTRIC FIELD ON LOCAL STRUCTURE OF BARIUM TITANATE
SINGLE CRYSTAL STUDIED BY X-RAY ABSORPTION SPECTROSCOPY
TECHNIQUE. THESIS ADVISOR : ASSOC. PROF. RATTIKORN
YIMNIRUN, Ph.D. 77 PP.

BARIUM TITANATE/SINGLE CRYSTAL/X-RAY ABSORPTION

In this work, effect of temperature and electric field on local structure of barium titanate single crystal was studied the single crystals used in this work were grown by Remeika process. To investigate the effect of temperature on the local structure in BaTiO$_3$ single crystals, the samples were heated to 50, 100, 120 130 and 150°C. To examine the influence of applied electric field on the local structure in BaTiO$_3$ single crystals, the samples were applied with the external electric field in steps: without electric field, applied 0.5Ec, 1Ec and 1.5Ec (Coercive Electric Field (Ec) = 1.7 kVdc/cm). The results showed that an increasing of temperature lead to the phase transition from tetragonal to cubic perovskite in BaTiO$_3$ crystal. The local structure also showed the similar transition behavior. In addition, the effect of the applying electric field displaced Ti atoms from central of perovskite BaTiO$_3$ unit cell. The results were confirmed by FeFF 8.2 calculations.

School of Physics   Student's Signature _____

Academic Year 2016   Advisor's Signature _____

                                     Co-advisor's Signature _____

ACKNOWLEDGEMENTS

CONTENTS

CONTENTS (Continued)

CONTENTS (Continued)

LIST OF TABLES

LIST OF FIGURE

LIST OF FIGURE (Continued)

LIST OF FIGURE (Continued)

LIST OF FIGURE (Continued)

LIST OF ABBREVIATION

BT	Barium titanate
S	Spin
BL5.2	Beamline 5.2
°C	Degree Celcius
DOS	Density of State
E_c	Coercive field
E_0	Absorption edge
eV	Electron-volt
h	Plank's constant
i	Current density
I_e	Electron current
I_p	Photon current
MPB	Morphotropic phase boundary
λ	Wave length
SCF	Self consist field
FMS	Full-Multiple Scattering
FWHM	Full Width at Half Maximum
SEM	Scanning Electron Microscopy
SLRI	Synchrotron Light Research Institute
XRD	X-ray Diffraction
XAS	X-ray Absorption Spectroscopy

LIST OF ABBREVIATION (Continued)

XANES	X-ray Absorption Near-Edge Structure
EXAFS	Extended X-ray Absorption Fine Structure

CHAPTER I

INTRODUCTION

1.1 Background

Barium titanate ($BaTiO_3$) has a relatively simple crystal structure and a rich ferroelectric and structural phase diagram. It has been one of the most extensively studied ferroelectric materials since its discovery as a ferroelectric in 1946. $BaTiO_3$ has been of practical interest for more than 65 years because of its attractive properties (Vijatović et al., 2008). Firstly, it is chemically and mechanically very stable; secondly, it exhibits ferroelectric properties at and above room temperature; and finally, it can be easily prepared and used in the form of ceramic polycrystalline samples. Due to its high dielectric constant and low loss characteristics, barium titan ate has been used in applications, such as capacitors and multilayer capacitors (MLCs). Doped barium titanate has found wide applications in semiconductors, PTC thermistors and piezoelectric devices (Wang et al., 2010).

Effect of temperature on the global structure of $BaTiO_3$ has long been studied. The researchers have found that $BaTiO_3$ has the perovskite structure in nature. At room temperature, it has a tetragonal phase and at the Curie's temperature, it changes to a cubic phase (Ravel et al., 1998). Interestingly, the effect of electric field on the local structure has recently been studied. When applied with electric field, the Ti atom in perovskite structure will be distorted and $BaTiO_3$ exhibits increasing polarization (Shieh et al., 2009).

In this work, X-ray absorption spectroscopy (XAS) technique, as proven very powerful and suitable for investigating the local structure, will be employed to study the effect of temperature and electric field on the local structure of Ti atoms in $BaTiO_3$ single crystal with the perovskite structure.

1.1.1 Barium titanate

Barium titanate is a dielectric material with the chemical formula $BaTiO_3$. The structure of $BaTiO_3$ is tetragonal perovskite-like structure, which is a network of corner-linked oxygen octrahedra, with the Ti atoms within the octrahedral hole and the Ba atoms filling the dodecahedral hole, as shown in Figure 1.1 The $BaTiO_3$ was first developed as piezoelectric ceramic, and it still is widely studied in the family of perovskite-like dielectric materials (Wei and Yao, 2007). Moreover, it has been mostly applied in multilayer ceramic capacitors.
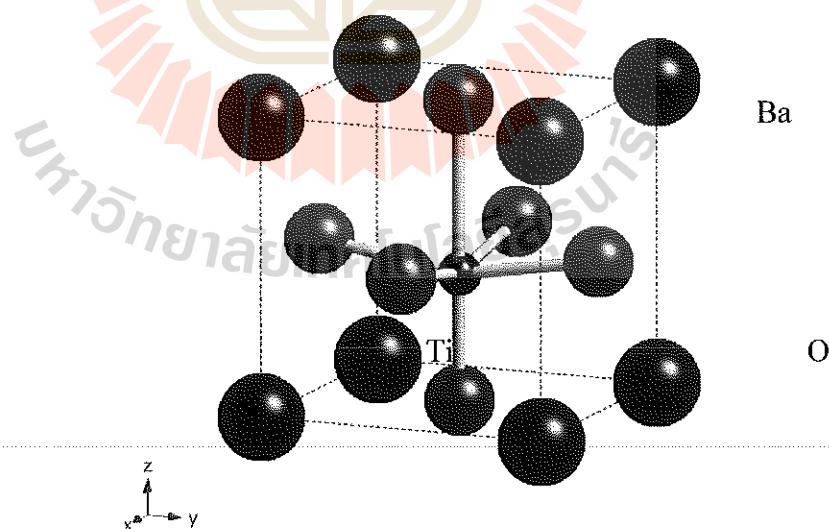
Figure 1.1 Crystal structure of tetragonal perovskite $BaTiO_3$ (Bootchanont, 2015).

Barium titanate is known to exhibit phase transition in bulk forms with various temperatures (T). At $T \leq -90°C$, the structure of $BaTiO_3$ is trigonal or rhombohedral, between $-90°C$ to $5°C$, the rhombohedral structure change to orthorhombic. Above $5°C$, the orthorhombic cell changes to tetragonal and the tetragonal, changes structure to cubic cell at Curie temperature (T_C) about $120°C$ (Maiti et al., 2008). In addition, the structure of $BaTiO_3$ is tetragonal at room temperature; the titanium ion is off-center which is resulting in the distortion of TiO_6 octrahedra when the temperatures lower than Curie temperature. The distorted of Ti in oxygen octrahedra create a very large spontaneous polarization, and in tune dielectric constant. Moreover, it can be reversed by applying a suitable electric field E or coercive electric field (E_c) (A. Bootchanont et al., 2015).

1.1.2 Phase transitions of barium titanate

Barium titanate is the first discovered ferroelectric perovskite. Its ferroelectric properties are connected with a series of three structural phase transitions by the effect of temperatures. The Curie point T_C, of barium titanate is $120°C$. Above $120°C$ the original cubic cell is stable up to $1460°C$. Above Curie temperature is a hexagonal structure where is stable (Cho, 1998). When the temperature is below the Curie point, crystallographic changes in $BaTiO_3$ occur, first at about $120°C$ a ferroelectric transition between the cubic, paraelectric and ferroelectric phase of tetragonal structure takes place. At $5°C$, the transition to a phase of the orthorhombic structure goes on and at $-90°C$ to the low temperature phase having a trigonal structure

(Koelzynski et al., 2005). Figure 1. 2 illustrates crystallographic changes of BaTiO₃ (Vijatović et al., 2008).
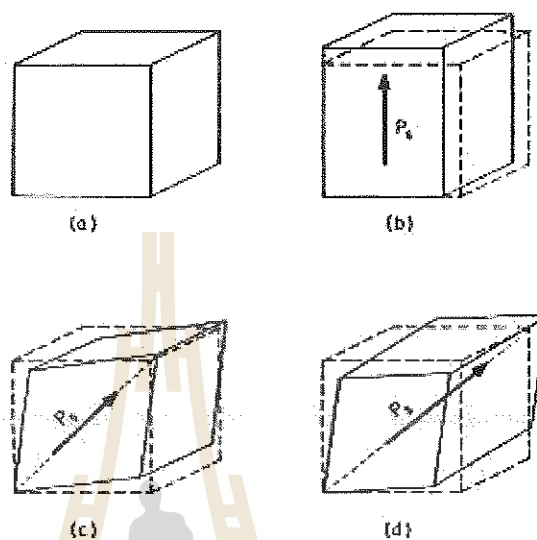
Figure 1.2 Unit cells of the four phases of BaTiO₃ :(a) Cubic, stable above 120°C, (b) Tetragonal, stable between 120°C and 5°C, (c) Orthorhombic, stable between 5°C and -90°C , (d) Rhombohedral, stable below -90°C, The dotted lines in (b), (c) and (d) delineate the original cubic cell (Vijatović et al., 2008).

At the Curie point, Ti-ions are all in equilibrium positions at the center of oxygen octahedra, but with a decrease of the temperature, Ti-ions jumps between energetically favorable positions out the of octahedron center, as shown in Figure 1.3 (Filho, 2006).
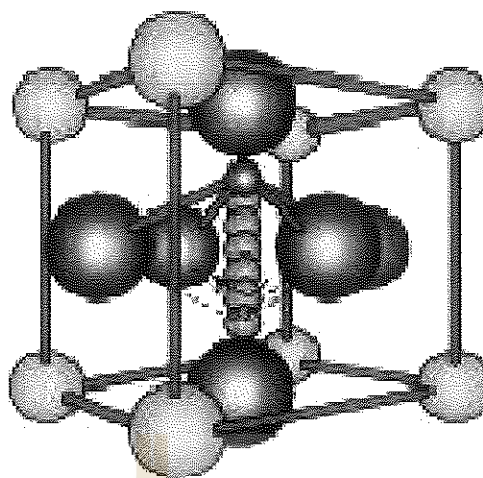
Figure 1.3 Ion positions in tetragonal BaTiO$_3$ (F.M. Filho, 2006).

These changes can be related to structural distortion, lengthening of the bonds or their shortening, so crystallographic dimensions of the barium titan ate lattice change with temperature. A lot of papers indicate that the mechanisms responsible for these phase transitions in BaTiO$_3$ are complex.
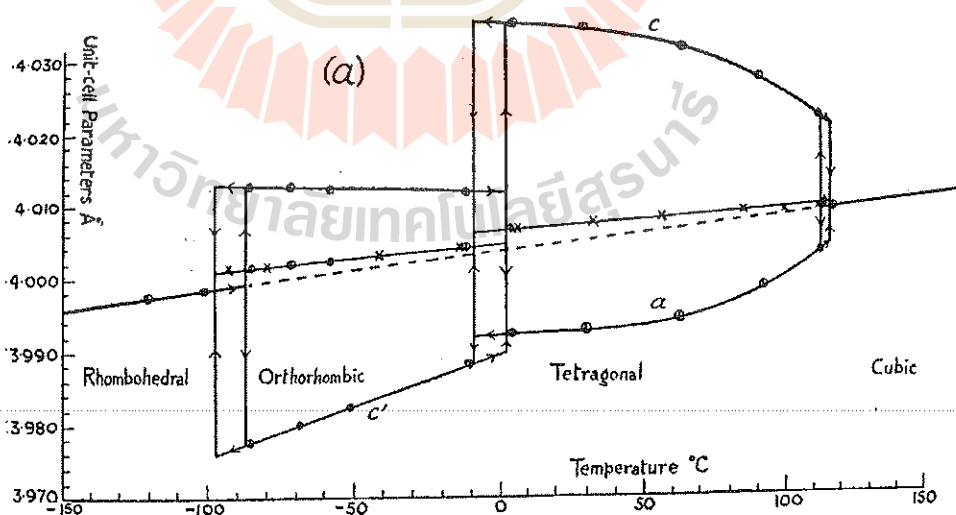
Figure 1.4 Lattice constants of BaTiO$_3$ as function of temperature. (Jona et al., 1993).

The temperature dependence of the lattice constants of $BaTiO_3$ in the four phases is depicted in Figure 1.4.

1.1.3 Electric field and polarization

The phenomenon of ferroelectricity was discovered in single-crystal materials of Rochelle salt (sodium tartarate tetrahydrate, $NaKC_4H_4O_6\ 4H_2O$) in 1921. The two conditions necessary in a material to classify it as a ferroelectric are the existence of spontaneous polarization and a demonstrated reorienting of the polarization (Haertling et al., 1999). Spontaneously polarized regions, with a single direction of polarization, are called domains. Orientation relationships between domains are governed by the crystal symmetry. The most outstanding feature of a ferroelectric ceramic is its hysteresis loop (i. e. a plot of polarization versus electric field, P-E). Figure 1. 5 illustrates a typical hysteresis loop.
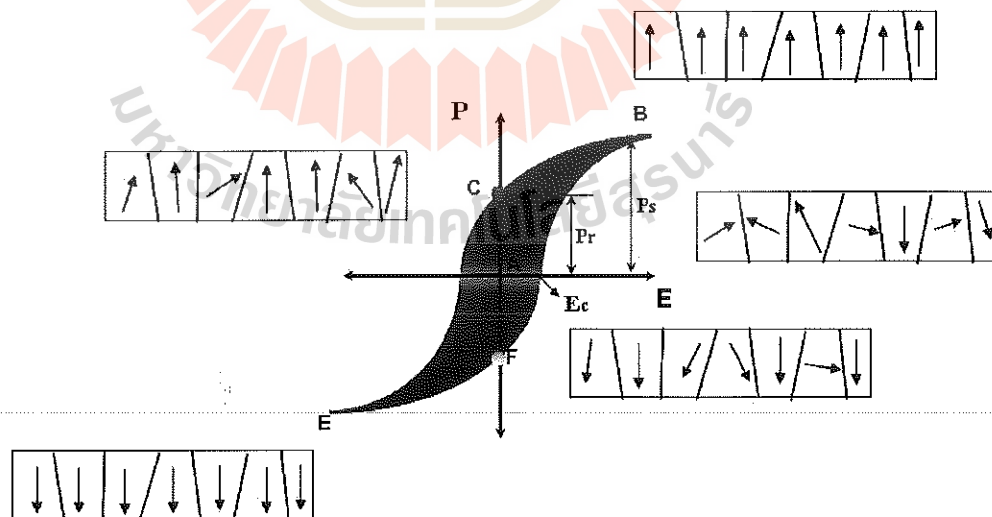
Figure 1.5 A typical P-E hysteresis loop in ferroelectrics. (Lazarevic et al., 2005).

When we apply an electric field, dipoles which are already oriented in the direction of the field will remain so aligned, but those which are oriented in the opposite direction will show a tendency to reverse their orientation, on the hysteresis loop that is a linear relationship between P and E and crystal behaves like a normal dielectric. When the electric field becomes sufficiently high to switch dipoles in crystallites, the polarization changes sharply and reaches saturation at higher fields. When the field is reduced to zero a net permanent polarization remains in the material known as remanent polarization, P_R. Extrapolation of the linear part of the curve back of the polarization axis represents the value of the spontaneous polarization, P_S. Reversing the electric field, polarization is reduced to zero and then changes sign as the field produced saturation polarization in the opposite direction, completing the cycle of the hysteresis loop. The value of the field required to reduce P to zero is called the coercive field E_C (Lazarevic et al., 2005).

In case of $BaTiO_3$ single crystals, it has only one domain in this crystal. When we apply an electric field, the Ti atom in perovskite structure will be moved off-center and the direction of Ti atom off-center correspond the direction of electric field, as shown in Figure 1.6.
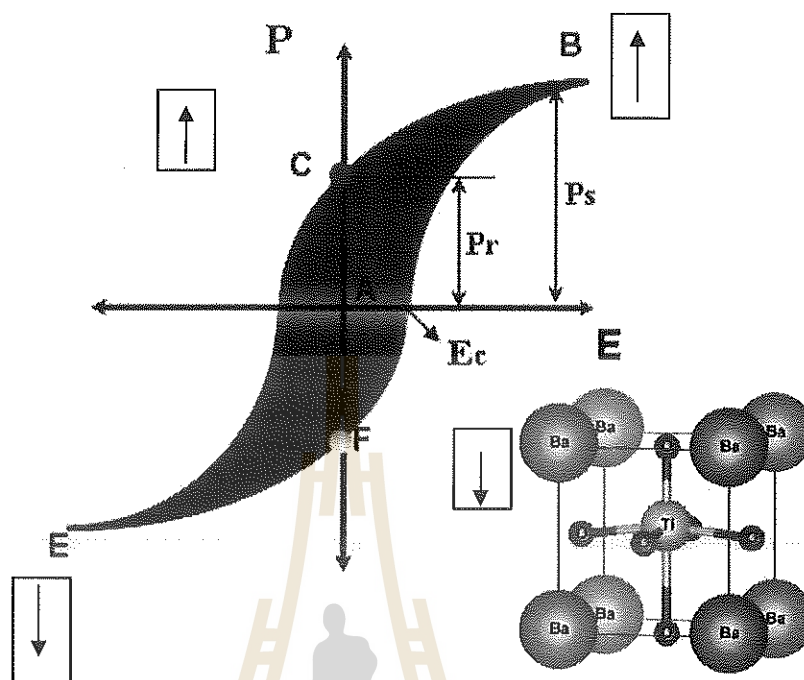
Figure 1.6 A typical P-E hysteresis loops in BaTiO$_3$ single crystals.

1.2 Research objectives

a) To study global structure of BaTiO$_3$ single crystals by XRD technique and microstructure by SEM technique.

b) To investigate effects of temperature on the local structure of BaTiO$_3$ single crystals by XAS technique.

c) To investigate effects of applied electric field on the local structure of BaTiO$_3$ single crystals by XAS technique.

1.3 Scope and limitation of the study

This work aims to study local structure of $BaTiO_3$ single crystals under the influence of temperature and applied electric field. The local structure of $BaTiO_3$ single crystals will be characterized by XAS. In addition, FEFF 8.2 code will be used to simulate the X-ray Absorption Near Edge Structure (XANES) spectra of $BaTiO_3$ single crystals and compare with measured spectra. Athena program will be used for data processing and data analysis.

CHAPTER II

THEORY AND LITERATURE SURVEY

In this chapter, experimental technique utilized in the thesis work will be reviewed. Firstly, X-ray diffraction (XRD) was used for the structural characterization of BaTiO₃ single crystal. Secondly, by the scanning electron microscope (SEM) was used for demonstrating the single crystals product. Next, the attention was focused to the study of local structure around specific atoms which can be done by using X-ray absorption spectroscopy (XAS) in both extended X-ray absorption fine structure (EXAFS) and X-ray absorption near-edge structure (XANES) regions. We will describe the general concept of those techniques and how to extract the result from experiments. Finally, the detail of XAS spectrum calculation will be discussed in the last section.

2.1 Review of literatures

The work of Z. Lazarevic (2015) shows the XRD results of sintered samples prepared by mechanochemical synthesis and by the Pechini process Figure 2.1. shows the formation of tetragonal phase of $BaTiO_3$, which is approved by the appearance of X-ray reflections at $2\Theta = 22.184, 31.49, 38.849, 45.152, 50.729, 56.075$ and $65.711\pm$ (JCPDS 05-0626).
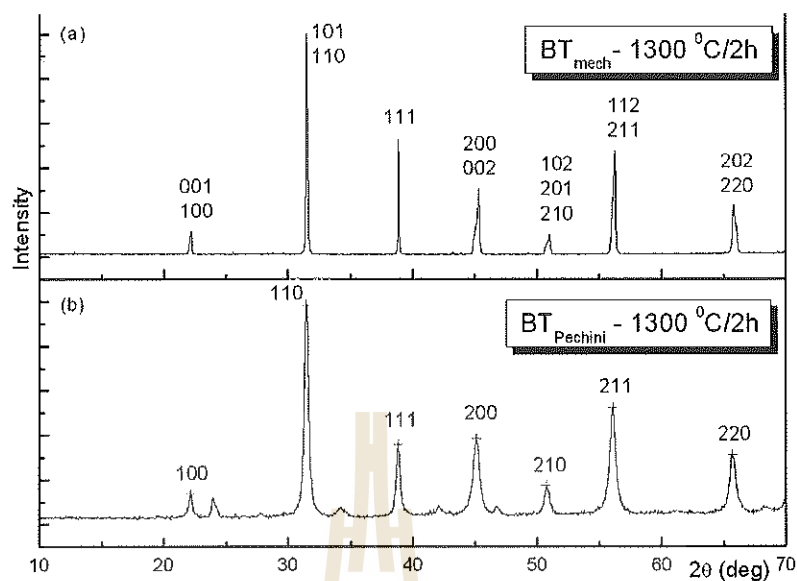
Figure 2.1 X-ray diffraction BaTiO$_3$ patterns obtained on sample sintered at 1300°C for 2 h and prepared by mechanochemical synthesis (a) and by Pechini method (b).

The work of Juyoung Kim demonstrates that the dielectric temperature characteristics of (Na0.5K0.5) NbO$_3$-doped BaTiO$_3$ (NKN–BT) were investigated through changes in the crystal structure and the local atomic structure. The dielectric constant of BaTiO$_3$ increased as temperature was increased from room temperature to the Curie temperature (Tc), and dramatically decreased after curie's temperature. The quantitative tetragonality (c/a) of the pure BaTiO$_3$ decreased from 1.007 to 1.000 with an increase in temperature, while the tetragonality of NKN–BT was in the range of 1.003–1.002 for the same temperature range. The extent of reduction of tetragonality for NKN–BT was lower than that for pure BaTiO$_3$ because of the TiO$_6$ octahedral distortion caused by the off-center shift of Ti. A local orientation change of the Ti atom from [001] to [111] direction with constant polarization, identi- fied by the pre-edge area analysis of the Ti K-edge, was apparent as a result of the NKN substitution.

The local polarization effect of NKN–BT attributed as the cause for the enhancement in dielectric constant to the range of 1406–1711. The distortion of TiO_6 octahedra by the orientational changes in Ti atoms, improved the thermal stability and dielectric constant over a temperature range of -25°C to +160°C.

The work of W. Kempet (2013) shows that PZT ceramic was studied by in-situ XAS technique. The in-situ technique was applied to determine the distortion of Ti atom position of PZT ceramic under an electrical field.

2.2 X-ray absorption spectroscope (XAS)

X-ray absorption Spectroscopy (XAS) is one of the powerful techniques to examine the electronic structure of materials, formal oxidation state, coordination number and used to probe local structure. The XAS experiment is normally carried out at the synchrotron radiation facility, which can be modified and selected the energy of X-ray photon (Koningsberger and Prins, 1988).

X-ray absorption spectroscope measures the X-ray absorption $\mu(E)$ as a function of X-ray energy

$$E = \hbar\omega.$$

(2.1)

The X-ray absorption coefficient is determined from the decay in the X-ray intensity I with the length of a sample x by the relationship,

$$I = I_0 e^{-\mu x},$$

(2.2)

where I_0 is the intensity of the incoming X-ray beam, I is the intensity of the beam after pass though the sample, and x is the thickness of the sample, μ is the definition of absorption coefficient, as shown in Figure 2.2.

$$I_0 \qquad I = I_0 e^{-\mu x}$$
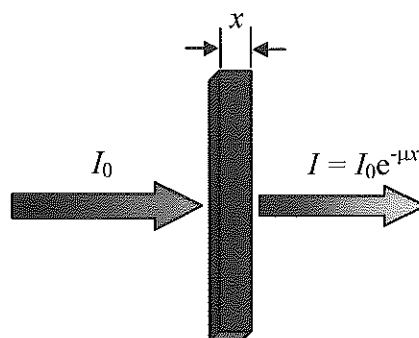
Figure 2.2 Schematic view of X-ray absorption measurement in transmission mode.

In the X-ray absorption process, a photon is absorbed by the atom, giving rise to the transition of the electrons from the inner shells: K, L or M shell to empty state above the Fermi level. The core hole, empty state, will be created in the inner shell, and the energy level of the shell is used to identify the type of absorption edge as shown in Figure 2.3. For example, K-edge refers to transition that excited electron from 1s shell to unoccupied states. The X-ray photon energy has to greater than the difference of energy between unoccupied states and K shell state. The energy of the absorption edges are specific characteristic to elements, making X-ray absorption an element-selective technique.
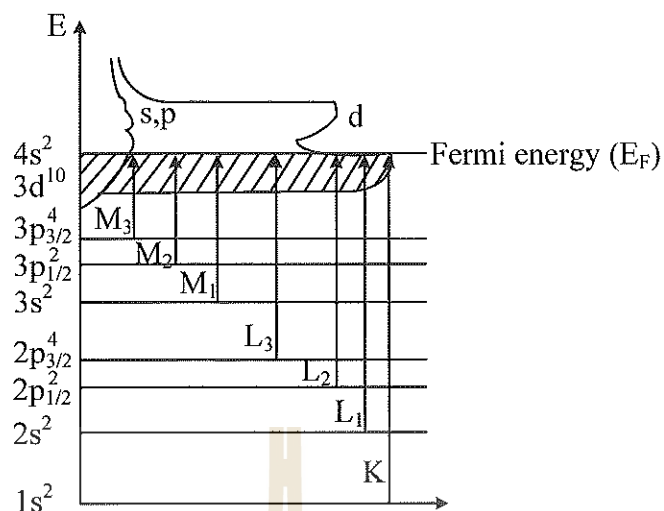
Figure 2.3 The relationship between the energy transitions and absorption edges [adapted from (Rehr and Albers, 2000)].
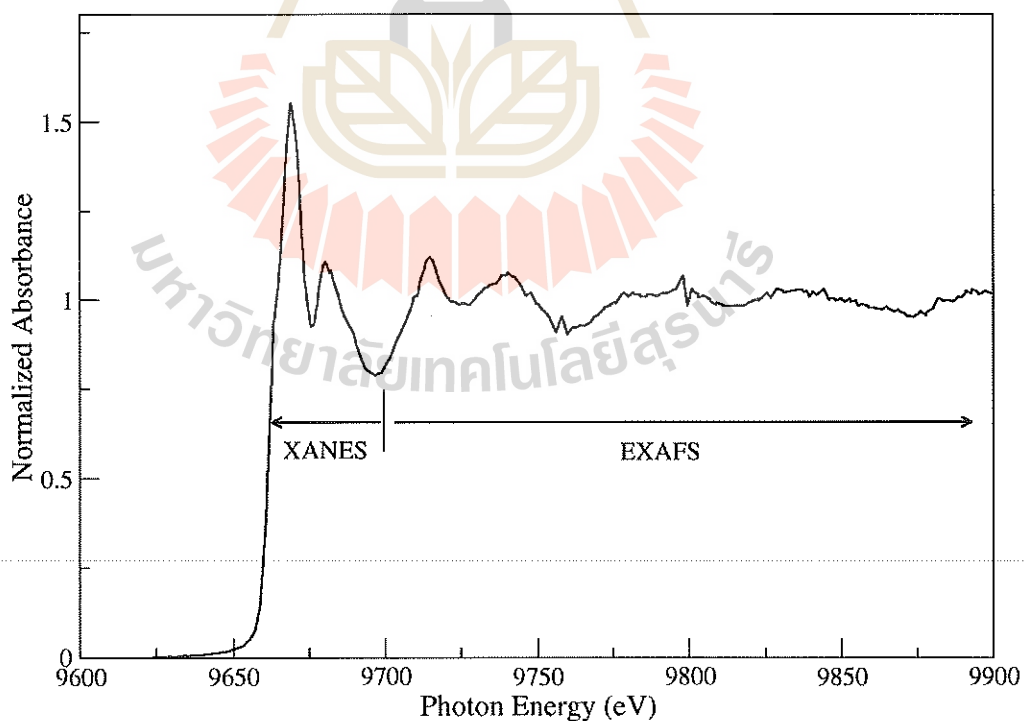
Figure 2.4 Normalize Zn *K*-edge absorption spectra classified into two regions; XANES and EXAFS.

The X-ray absorption spectrum is typically separated into two regions (1) the X-ray absorption near edge structure (XANES) which includes features approximately 50 eV above the absorption edge and (2) the extended X-ray absorption fine structure (EXAFS) typically extending to 1,000 eV above the absorption edge as shown in Figure 2.4.

2.2.1 X-ray absorption near edge structure (XANES)

X-ray absorption near edge structure, or XANES contains the information about the chemical state of the element, including the oxidation state, and the local geometry of the absorbing atom. XANES structure in an absorption spectrum cover the range between the threshold and the point at which the extended x-ray absorption fine structure (EXAFS) being. XANES comprises that part of the spectrum within about 40-50 eV of the edge.

This region of the absorption spectrum is dominated by multiple scattering of low energy of photoelectron. In addition there are normally strong features due to transitions to empty bonding and anti-bonding orbitals in molecular systems, or to atomic-like or unoccupied density of state in solid state systems. The combination of these influence mean that XANES is sensitive to the local electronic structure of the absorbing species and the coordination geometry. XANES has most often been used in a fingerprint fashion, with spectra compared to standards to determine the quantity of interest such as the oxidation state of the absorbing element.

The absorption coefficient in equation (2.5) is proportional to the transition rate as given by Fermi's Golden Rule; described by

$$\tilde{\mu}(E) \propto \sum_{f} \left| \left\langle f \left| \hat{\varepsilon} \cdot \vec{r} \right| i \right\rangle \right|^2 \delta\left(E_i - E_f + \hbar\omega \right) , \tag{2.5}$$

Where $|i\rangle$ is the initial core *ket* state vector, $\langle f|$ is the final *bra* state vector of the excited electron, E is the energy of absorbed x-ray photon, E_i is the energy of initial state, E_f is the energy of final state, $\hbar\omega$ is the energy of x-ray photon energy, $\hat{\varepsilon}$ is the x-ray polarization vector and $\tilde{\mu}(E)$ is absorption coefficient with ignoring of core hole life time and experimental resolution (Ankudinov et al., 1998). By considering Eq. further with the additional effects of core-hole lifetime and experimental resolution, the XANES spectra can be calculated as described later in section 2.3.

2.2.2 Extended X-ray absorption fine structure (EXAFS)

The extended x-ray absorption fine structure is the oscillating part of the x-ray absorption spectrum that extends to about 1,000 eV above the absorption edge. Analyses of the EXAFS spectrum provide information about the number, species and inter-atomic distances of the neighbors from the absorption atom. EXAFS is a result of the adjustment of the photoelectron final state due to scattering by the surrounding atoms. The final state photoelectron is changed to first order by a single scattering from each surrounding atom. According to quantum theory this photoelectron can be visualized as a wave emitted form the absorber with wavelength λ is given by the de Broglie relation in equation (2.6). In EXAFS region, the momentum of the photoelectron p can be defined by the free electron relation

$$\frac{p^2}{2m} = hv - E_0 , \tag{2.6}$$

where hv is the energy of frequency v photon, E_0 is the bonding energy of the photoelectron and m is mass of the excited electron.

For a solitary atom the photoelectron can be revealed as an outgoing wave as shown in Figure 2.5 by the solid line of Mg atom. The outing wave is scattered by

neighbor that surround the absorbing atom and generate scattered wave, which display by the dashed lines of O atoms. The final state is the superposition of the outgoing and scattered waves. Interference occurs between the outgoing and the backscattered waves and then creates the total amplitude. The total amplitude of the electron wave function would be raised or diminished, respectively, thus altering the possibility of absorption of the x-ray correspondingly. The phase change with the wavelength of the photoelectron depends on the distance between the center atom and backscattering atom. The variation of the backscattering strength as a function of energy of the photoelectron depends on the type of atom doing the backscattering. Thus EXAFS contains information on the atomic surroundings of the center atom.
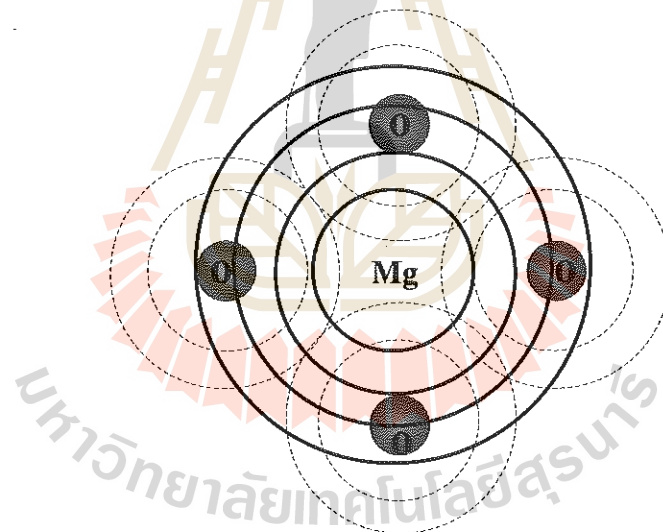
Figure 2.5 Schematic of the radial portion of the photoelectron wave.

The oscillatory part of the x-ray absorption above a given absorption edge, EXAFS function can be defined by

$$\chi(E) = \frac{\left[\mu(E) - \mu_{\circ}(E)\right]}{\Delta\mu_{\circ}},$$

(2.7)

where μ(E) is the x-ray absorption coefficient, μ_0(E) is smooth atomic background absorption coefficient.

Furthermore, in the EXAFS analysis $\chi(E)$ could be transformed from E space to k space by the relations $k = \sqrt{2m(E - E_0)/\hbar^2}$ Then the function can be converted from $\chi(E)$ to $\chi(k)$ for general purpose. In theoretical procedure, the $\chi(k)$ can be described by (Wilson et al., 2000)

$$\chi(k) = \sum_j \frac{S_o^2 N_j}{k R_j^2} \left| f_j(k, \pi) \right| \sin\left[2kR_j + \varphi_j(k) \right] e^{-2\sigma_j^2 k^2} e^{-2R_j/\lambda(k)} \quad , \quad (2.8)$$

Where Nj is the number of neighbor in J^{th} shell of surrounding atoms, k is photoelectron wave vector, f_j is the scattering amplitude, $S_o^2(k)$ is the amplitude eduction term due to many-body effect, R_j is radial distance from absorbing atom to J shell, $\lambda(k)$ is electron mean free path, σ_j is the Debye-Waller factor and $\varphi(k)$ accounts for the total phase shift of the curve wave scattering amplitude along the scattering trajectory.

The distance between core atom and backscattering atoms or the path-length change the phase contrasting with the wavelength of photoelectron. Furthermore, different types of surrounding atoms vary the backscattering intensity as a function of photoelectron energy. It is accepted that, by the careful analysis of the EXAFS structure, one can receive significant structural parameters surrounding the center atom.

2.2.3 Ti K Pre- edge XANES analysis

The integrated intensity of Ti K pre-edge, which is associated with both the quadrupole and the dipole 1s ⟶ 3d transition of Ti, reflects the $3d$-$4p$ hybridization for Ti. This hybridization results from displacement of the Ti atom from centro-

symmetric position within the oxygen octahedron. Vedrinskii et al. (1998) have shown that a contribution to the area under peak X is given by

$$A = \frac{\gamma_s}{3} d_s^2 \qquad (2.9)$$

In this equation, d_s is the mean-square displacement of Ti atom from center and a is the average displacement of the oxygen octahedral and A is a peak area. An experimental determination of the constant γ_s by Ravel (1998) resulted in values of 11.2 eV/Å² for BaTiO₃ with an error bar of about ±3 eV/Å² as shown in Figure 2.6.
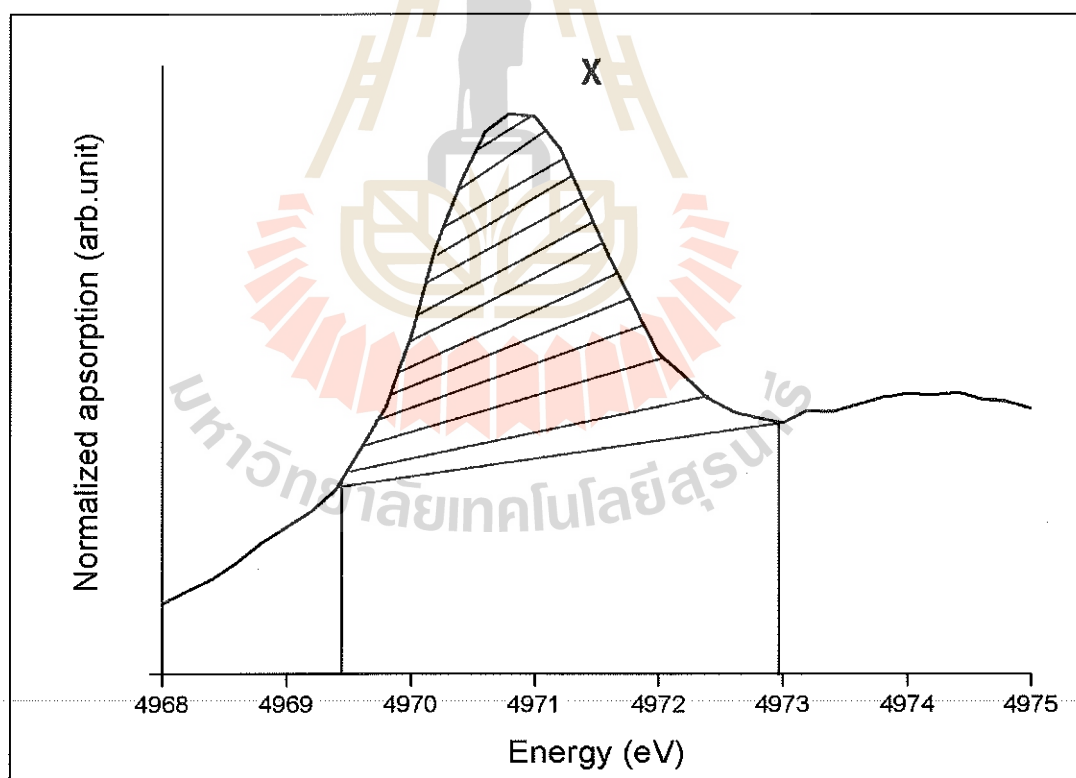
Figure 2.6 The Ti K pre-edge XANES of BaTiO₃ single crystal showing the calculated area under the spectral peak. (Adapt from Vedrinskii et al., 1998)

2.3 X-ray absorption spectrum calculation

2.3.1 FEFF code overview

In thesis, the principle theoretical calculations are performed based on FEFF 8.2 code. This code is developed to primarily calculate X-ray absorption for the FEFF (f_{eff}) project developed by the Department of Physics, University of Washington, Seattle. USA. Apart from XAS spectra calculation, FEFF code can also calculate X-ray natural circular dichroism (XNCD), spin-dependent calculations of X-ray magnetic dichroism (XMCD), nonresonent X-ray emission (XES) and electronic structure including local densities of states (LDOS). FEFF code is written in ANSI FORTRAN 77 with principle investigator John J. Rehr and co-principle investigator Alexei L. Ankudinov.

FEFF is ab intio self-consistent real space multiple-scattering (RSMS) code for simultaneous calculations of X-ray absorption spectra and electronic structure. The input file "feff.inp" can be created directly form ATOMS code via "atoms.inp" as shown in Figure 2.7.
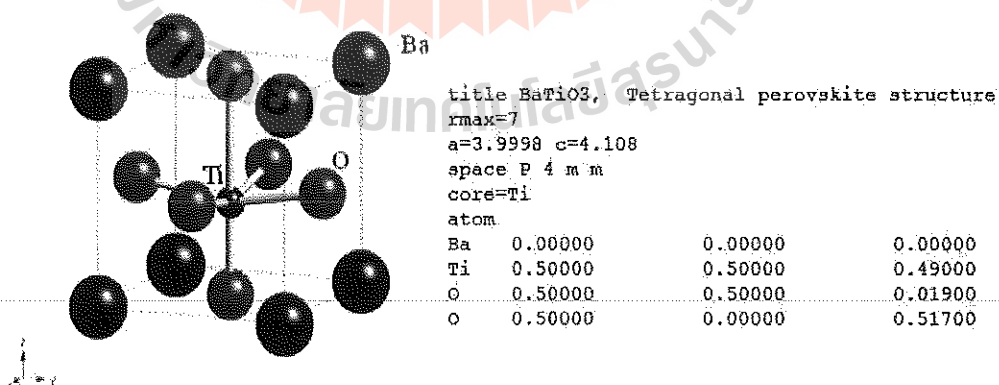
Figure 2.7 Detail of an atoms.inp input file to generate "feff.inp" for FEFF calculation.

```
TITLE     BaTiO3,   Tetragonal perovskite structure

EDGE      K
S02       1.0

*         pot   xsph   fms    paths genfmt ff2chi
CONTROL   1     1      1      1     1      1
PRINT     1     0      0      0     0      0

*         r_scf  [ l_scf  n_scf  ca ]
SCF       4.3    0       20      0.1

*         ixc  [ Vr   Vi ]
EXCHANGE  0      4    0.3

*EXAFS
*RPATH    8.50057

*         kmax  [ delta_k  delta_e ]
XANES     7.0    0.05      0.3
*         r_fms       [ l_fms ]
FMS       6.5    0
*
RPATH     0.10000
*         emin   emax  resolution
*LDOS     -20    20    0.1

POTENTIALS
*   ipot   z [ label   l_scmt   l_fms   stoichiometry ]
    0      22   Ti       -1       -1        0
    1      8    O        -1       -1        3
    2      56   Ba       -1       -1        1
    3      22   Ti       -1       -1        1

ATOMS
   0.00000      0.00000      0.00000    0   Ti        0.00000
   0.00000      0.00000     -1.93195    1   O         1.93195
   0.00000     -1.99990      0.11075    1   O         2.00296
   1.99990      0.00000      0.11075    1   O         2.00296
  -1.99990      0.00000      0.11075    1   O         2.00296
   0.00000      1.99990      0.11075    1   O         2.00296
   0.00000      0.00000      2.16985    1   O         2.16985
   1.99990      1.99990     -2.00988    2   Ba        3.46970
  -1.99990     -1.99990     -2.00988    2   Ba        3.46970
  -1.99990      1.99990     -2.00988    2   Ba        3.46970
   1.99990     -1.99990     -2.00988    2   Ba        3.46970
  -1.99990     -1.99990      2.09192    2   Ba        3.51786
  -1.99990      1.99990      2.09192    2   Ba        3.51786
   1.99990      1.99990      2.09192    2   Ba        3.51786
   1.99990     -1.99990      2.09192    2   Ba        3.51786
```

Figure 2.8 Detail of a "feff.inp" input file of $BaTiO_3$ with Ti as center atom for FEFF calculation.

The suitable commands, parameter and atomic positions for FEFF-XAS spectrum calculations can be edited within the input file named "feff.inp", which is shown in Figure 2.8. This file controlled with some details, for instance the generator of input file and the number of atom which is contain in the cluster. The followed

details describe about various card use to assign the steps of calculation. The type of atomic potentials and defined atomic symbols are presented in the next part, and eventually with the locations of the created atoms in the system where the location of center atom is placed at (0,0,0) in (x,y,z) coordination.

2.3.2 XAS Calculation

Calculation of XAS can be carried out with the imaginary part of one-electron Green's function operator (Ankudinov, 1998)

$$G = [E - H]^{-1},$$ (2.10)

where H is the effective one-electron operator Hamiltonian and E is the photoelectron energy. Based on the Green's-function calculation in the complex plane, to explicit equation (2.10) by using spectral representation with Green-function operator, thus the absorption coefficient can be rewritten as

$$\tilde{\mu}(E) \propto -\frac{2}{\pi} \operatorname{Im} \langle i | \hat{\varepsilon} \cdot \vec{r}' G(\vec{r}', \vec{r}, E) \hat{\varepsilon} \cdot \vec{r} | i \rangle$$ (2.11)

Where $G(\vec{r}', \vec{r}, E) = \langle \vec{r}' | G(E + in) | \vec{r} \rangle$, $\hat{\varepsilon}$ is the x-ray polarization vector and the parameters denoted with prime is that quantity in final state (Ankudinov, 1998). Furthermore, since only the transition to unoccupied state above Fermi energy are permitted and the effect of core-hole lifetime and experimental resolution are essentially taken in to calculation, the total absorption coefficient should become

$$\mu(E) = \int_{E_F}^{\infty} dE' \tilde{\mu}(E') \frac{\Gamma}{\pi[(E - E')^2 + \Gamma^2]},$$ (2.12)

where Γ is determined by the combined sum of the core-hold life time and experimental resolution, and E_F is Fermi level energy. FEFF code aids scientist to approach the XAS spectra by performing the possibly precise Green's function in $\tilde{\mu}(E)$. For FEFF 8 series, the developers suggested two mains developed feature for XAS calculation. The two main advantages are the approaches of self-consistent field (SCF) and full multiple scattering (FMS).

For XAS calculation (especially XANES), the SCF loops are used to create the SCF potentials and compute the total electron density and Coulomb potential within RSMS Green's-function framework. In FEFF 8.2 code, the SCF potentials are implemented using the spherical or "muffin-tin potential" as illustrated in Figure 2.9. Muffin-tin potential considers the atomic interval potential since a spherical scattering potential center on each atom equal to sum of overlapping potential and has a constant value in the interstitial region between atoms. FMS card will perform the calculation for all possible paths within the defined cluster.

(a) (b)
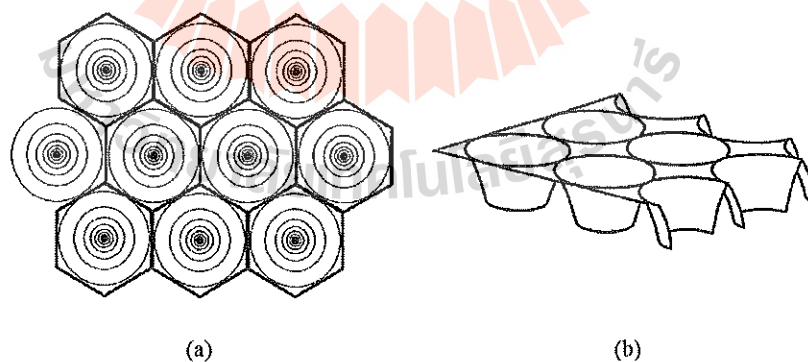
Figure 2.9 Schematic illustration of muffin-tin potential in two dimensions (Rehr and Albers, 2000).

The SCF loop constructs Green's function, which consist of central atom and scattering contribution

$$G(\vec{r}, \vec{r}', E) = G^c(\vec{r}, \vec{r}', E) + G^{sc}(\vec{r}, \vec{r}', E), \qquad (2.13)$$

where $G^c(\vec{r}, \vec{r}', E)$ and $G^{sc}(\vec{r}, \vec{r}', E)$ are central and scattering contribution, respectively.

XANES calculation can be performed under the defined control cards, most of them are normally used as the defaults, excepting FMS and SCF which are importantly managed. For SCF consideration, the cluster radius is used to define the suitable scattering potential, which usually requires around 30 atoms within the cluster. That cluster radius should be defined at the consistent of calculated absorption spectra

2.4 X-ray diffractometry (XRD)

X-ray Powder Diffraction is a one of the standard techniques that can be used to identify the crystal structure of materials. Fundamental treatment of X-ray diffraction by crystals is done by considering the interaction of an X-ray plane wave with the electrons of the crystal materials (Guinier, 1994). The wave nature of the x-rays means that they are reflected by the lattice of the crystal, as shown in Figure 2.10, to give a unique pattern of peaks of "reflections" at differing angles and of different intensity, just as light can be diffracted by a grating of suitably spaced lines. The diffracted beams from atoms in successive planes cancel unless they are in phase, and the condition for this is given by the Bragg relationship;

$$2d \sin\theta = n\lambda, \qquad (2.14)$$

where d is the distance between adjacent planes of atoms, θ is the angle of incidence of the X-ray beam, n is the order of the diffracted beam and λ represents the wavelength of the incident x-ray beam.
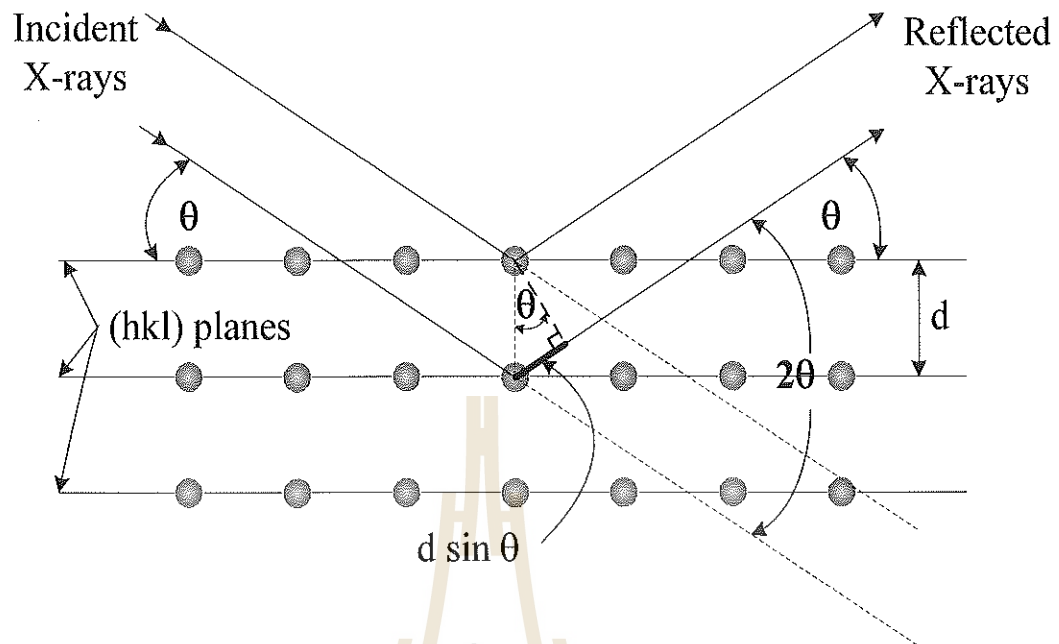
Figure 2.10 The X-ray diffraction beam path.

The Bragg condition can be satisfied for any set of planes whose spacing is greater than half the wavelength of the x-ray used (if $d < \lambda/2$, then $\sin\theta > 1$, which is impossible). This condition sets a limit on how many orders of diffracted waves can be obtained from a given crystal using an x-ray beam of a given wavelength. Since the crystal pattern repeats in three dimensions, forming a three-dimensional diffraction grating, three integers, denoted ($h\ k\ l$) are required to describe the order of the diffracted waves. These three integers are defined as the Miller indices which used in crystallography, denote the orientation of the reflecting sheets with respect to the unit cell and the path difference in units of wavelength between identical reflecting sheets.

The Miller indices ($h\ k\ l$) can be calculated from Bragg's law:

$$2d_{hkl} \sin\theta = n\lambda .$$

(2.15)

In the cubic systems, the plane spacing is related to the lattice parameter and the Miller indices by the following relation:

$$d_{hkl} = \frac{a}{\sqrt{h^2 + k^2 + l^2}} .$$

(2.16)

Combining equation (2.15) and (2.16), we get

$$a_{hkl} = \frac{n\lambda\sqrt{h^2 + k^2 + l^2}}{2\sin\theta} .$$

(2.17)

Considering the non cubic systems such as hexagonal system, the Miller indices can be calculated by using the lattice parameter from Bravais lattice:

$$\frac{1}{d^2} = \frac{4}{3}\left(\frac{h^2 + hk + k^2}{a^2}\right) + \frac{l^2}{c^2} .$$

(2.18)

Recall Bragg's law:

$$2d\sin\theta = \lambda,$$

(2.19)

$$4d^2\sin^2\theta = \lambda^2,$$

(2.20)

$$\frac{1}{d^2} = \frac{4\sin^2\theta}{\lambda^2} .$$

(2.21)

Combining equation (2.20) and (2.21), we obtain

$$\frac{1}{d^2} = \frac{4}{3}\left(\frac{h^2 + hk + k^2}{a^2}\right) + \frac{l^2}{c^2} = \frac{4\sin^2\theta}{\lambda^2} .$$

(2.22)

We can rearrange equation (2.21) in term of $\sin^2\theta$ as,

$$\sin^2\theta = \left(\frac{\lambda^2}{4a^2}\right) * \left[\frac{4}{3}(h^2 + hk + k^2) + \frac{l^2}{(c/a)^2}\right],$$

(2.23)

where a and c/a are constants for a given diffraction pattern.

The information of an XRD pattern can be used to approximate the crystallite size of particles by using Debye-Scherrer formula (Warren, 1969):

$$D = \frac{K\lambda}{\beta\cos\theta},$$ (2.24)

where D is crystalline size, λ is the wavelength of x-ray radiation (1.5418 Å for Cu K_α), β is the full wide at half maximum height (FWHM), K is the crystallite shape factor (usually taken as 0.89), θ is the diffraction angle.
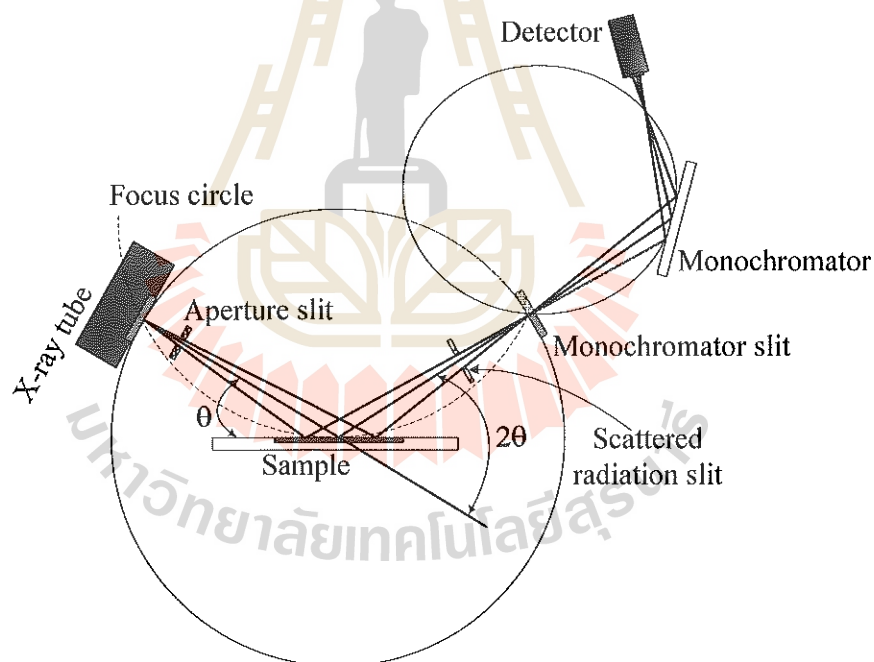
Figure 2.11 Schematic representation of X-ray diffractometer D5005 [adapted from (BRUKER, Analytical X-ray Systems, 1998)].

2.5 Scanning electron microscopy (SEM)

The scanning Electron Microscope (SEM) is an importance electron microscope that uses a focused beam of high-energy electrons to generate a variety of signals at the surface of solid specimens. The signals that derive from the interaction of the focused beam of high energy electrons with the atoms of the target sample reveal information about the sample including external morphology (texture), chemical composition, and crystalline structure and orientation of materials making up the sample (Brandon and Kaplan, 1999).

The schematic diagram of scanning electron microscope is shown in Figure 2.12. The SEM generates a beam of incident electrons in an electron column above the sample chamber. The electrons are produced by a thermal emission source, such as a heated tungsten filament, or by a field emission cathode. The energy of the incident electrons can be as low as 100 eV or as high as 30 keV depending on the evaluation objectives. The electrons are focused into a small beam by a series of electromagnetic lenses in the SEM column. Scanning coils near the end of the column direct and position the focused beam onto the sample surface. The electron beam is scanned in a raster pattern over the surface for imaging. The beam can also be focused at a single point or scanned along a line for x-ray analysis. The beam can be focused to a final probe diameter as small as about 10 Å. when the electron beam strikes a specimen, a large number of signals are generated. Theses signals include secondary electrons, backscattered electrons, characteristic x-ray, cathodeoluminescence and transmitted electrons, as shown in Figure 2.13.

Electron gun

Cathoad Ray Tube

Condenser lens

Scanning circult

Scanning coil

Objective lens

Video signal amplifier

Specimen

Signal detector
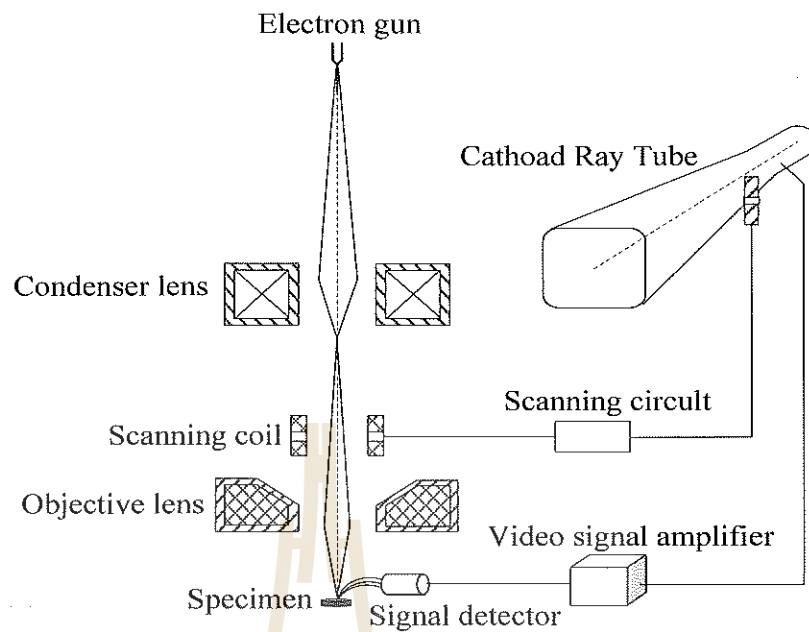
Figure 2.12 Principles schematic illustration of SEM (JEOL, Ltd., 1989).

Electrons
probe

Backscattered
electrons

Auger
electrons

X-ray

Cathodoluminescence

Secondary
electrons

Specimen

Elastically
scattered
electrons

Transmitted
electrons

InElastically
scattered
electrons
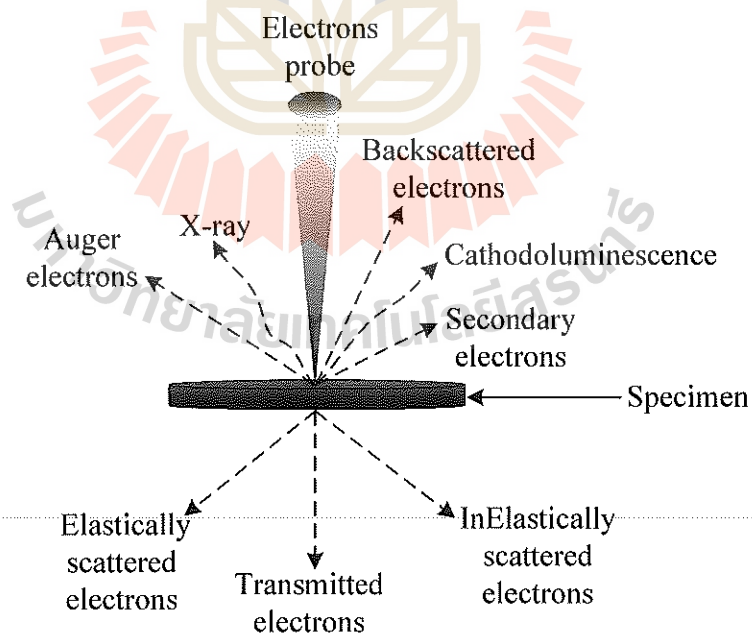
Figure 2.13 Schematic diagram of signals in SEM (JEOL, Ltd., 1989).

There are four the significant signals which to use in SEM (JEOL, Ltd., 1989):

1) Secondary Electrons (SE) are emitted lower-energy electrons, which can be formed by inelastic collisions with the nucleus where substantial energy loss occurs or by the ejection of loosely bound electrons from the sample atoms. The energy of secondary electrons is typically 50 eV or less. The topography of surface features influences the number of electrons that reach the secondary electron detector from any point on the scanned surface. This local variation in electron intensity creates the image contrast that reveals the surface morphology. The secondary electron image resolution for an ideal sample is about 3.5 nm for a tungsten-filament electron source SEM or 1.5 nm for field emission SEM.

2) Backscattered electrons are high-energy electrons that are ejected by an elastic collision of an incident electron, typically with a sample atom's nucleus. These high-energy electrons can escape from much deeper than secondary electrons, so surface topography is not as accurately resolved as for secondary electron imaging. The production efficiency for backscattered electrons is proportional to the sample material's mean atomic number, which results in image contrast as a function of composition, mean that higher atomic number material appears brighter than low atomic number material in a backscattered electron image. The optimum resolution for backscattered electron imaging is about 5.5 nm.

3) Characteristic x-rays are generated when the electron beam interacts with the inner shell electrons of the specimen atoms by inelastic scattering with enough energy to excite inner shell electrons to outer shell orbitals, leaving inner-shell vacancies. As outer-shell electrons fall to the various inner shell orbitals, characteristic amounts of energy are generated that are a function of the target element and the type of orbital

decay. These characteristic x-ray are used to identify the component and measure the plenty of elements in the sample.

4) Cathodoluminescence (CL), the emission of light when atoms excited by high-energy electrons come back to their ground state. In the SEM, CL detectors either collect all light emitted by the specimen, or can analyses the wavelengths emitted by the specimen and display an emission spectrum or an image of the distribution of cathodoluminescence emitted by the specimen in real color.

To create an SEM image, the incident electron beam is scanned in a raster pattern across the sample's surface. The emitted electrons are detected for each position in the scanned area by an electron detector. The intensity of the emitted electron signal is displayed as brightness on a cathode ray tube (CRT). By synchronizing the CRT scan to that of the scan of the incident electron beam, the CRT display represents the morphology of the sample surface area scanned by the beam. Magnification of the CRT image is the ratio of the image display size to the sample area scanned by the electron beam.

Two electron detector types are predominantly used for SEM imaging. Scintillator type detectors (Everhart-Thornley) are used for secondary electron imaging. This detector is charged with a positive voltage to attract electrons to the detector for improved signal to noise ratio. Detectors for backscattered electrons can be scintillator types or a solid-state detector. The SEM column and sample chamber are at a moderate vacuum to allow the electrons to travel freely from the electron beam source to the sample and then to the detectors. High-resolution imaging is done with the chamber at higher vacuum, typically from 10^{-5} to 10^{-7} Torr. Imaging of

nonconductive, volatile, and vacuum-sensitive samples can be performed at higher pressures.

Energy dispersive x-ray spectroscopy (EDS) is an analytical technique for identifying and quantifying elemental compositions in a very small sample of material. EDS is an integral part of the scanning electron microscope. When taking an SEM image, the surface under consideration is bombarded with an electron beam. A schematic of EDS system is depicted in Figure 2.14. The bombardment of electrons causes an excitation between the atoms, which results in a release of excess energy in the form of X-ray. When the samples surface is bombarded by the electron beam, some electrons are removed from the atoms on the sample surface. This results in electron vacancies which must be filled with electrons from a higher shell. As a result, an X-ray is emitted to balance the energy difference between the two electrons. The amount of energy released is characteristic of the atoms it excites, forming various peaks in the energy spectrum, according to the composition of the material. The intensities or areas of the various peaks of a specific spectrum are proportional to the concentration of that specific element, making EDS not only a qualitative but also a quantitative composition diagnostics tool.
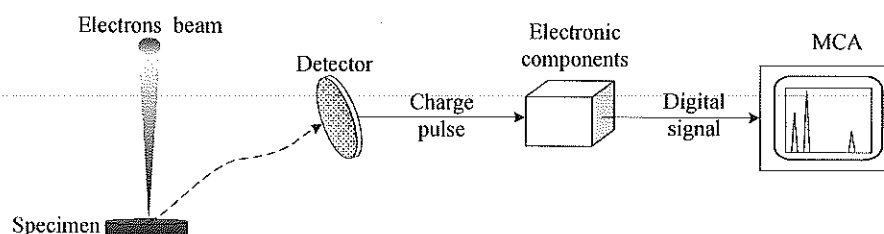
Figure 2.14 Schematic diagram of an EDS.

CHAPTER III

RESEARCH METHODOLOGY

To investigate the local structure, X-ray Absorption Spectroscopy (XAS) measurements were performed at BL-5.2 of the Siam Photon Laboratory, Synchrotron Light Research Institute (SLRI), Thailand (electron energy of 1.2 GeV, beam current 140-70 mA). The double-crystal monochromator was operated with a pair of Ge(220) crystals. The electron in Ti K-edge was excited with energy steps of 0.20 eV. The experiments were measured in fluorescence mode and the signals were corrected by 4-channal Si drift-detector. The X-ray Absorption Near-Edge Structure (XANES) measurements for the Ti K-edge were measured for all compositions in the energy range from 4950 eV to 5060 eV. The data were processed using the ATHENA program.

3.1 Research procedures

In this work, $BaTiO_3$ (BT) single crystals grown by Remeika process were provided by our collaborators (Edward et al., 2001). To investigate the effect of temperature on the local structure in $BaTiO_3$ single crystals, the single crystal samples were heated to 50, 100, 120 130 and 150°C. To examine the influence of applied electric field on the local structure in $BaTiO_3$ single crystals, the samples were applied with the external electric field in steps: without electric field, applied 0.5Ec, 1Ec and 1.5Ec (Coercive Electric Field (Ec) = 1.7 kVdc/cm).

Two standard characterizations, i.e. X-ray diffraction (XRD) and scanning electron microscope (SEM) images will be presented and discussed. Figure 3.1 shows the flow chart of research procedures.
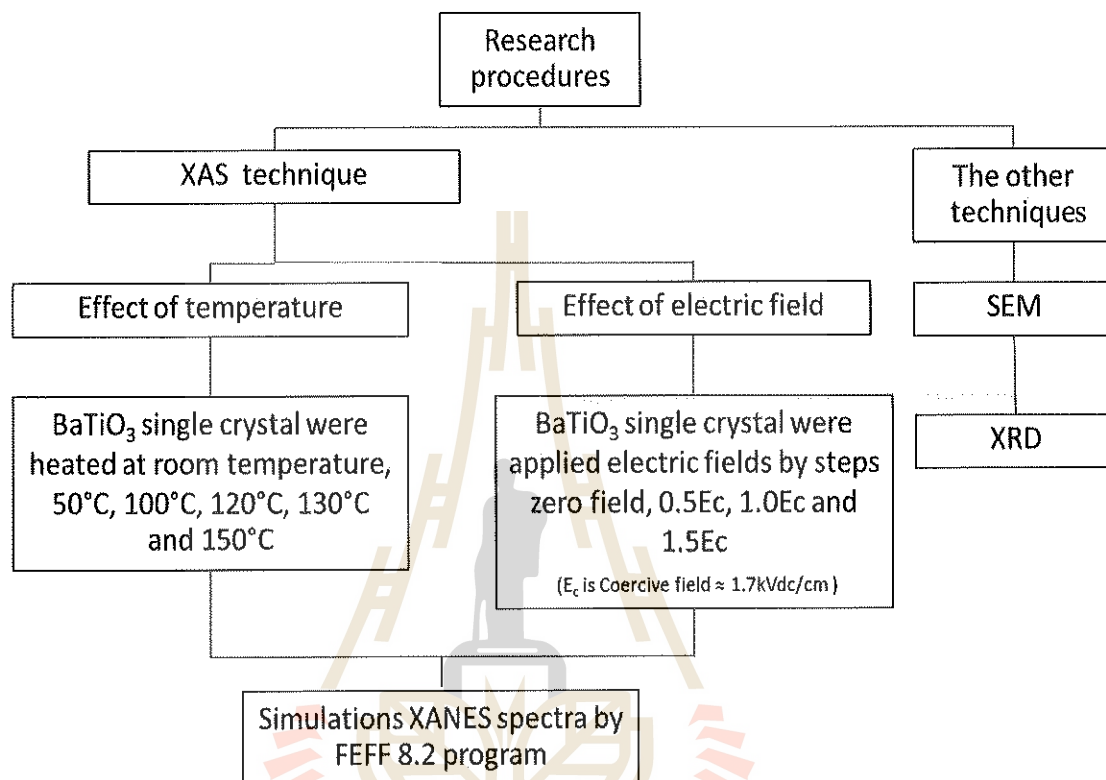
Figure 3.1 Flow chart of research procedures.

3.2 X-ray absorption Spectroscopy (XAS) setup

The X-ray absorption spectroscopy experiment is commonly accomplished at a synchrotron radiation source, due to high intensity and energy alterable competency of generated X-ray photon, and the competency to obtain the continuous absorption spectrum over extensive energy range. In general, there are three types of X-ray absorption measurements: transmission-mode XAS, fluorescence-mode XAS and electron-yield XAS as schematic illustration shown in Figure 3.2.

sample

(a)

(b)

(c)
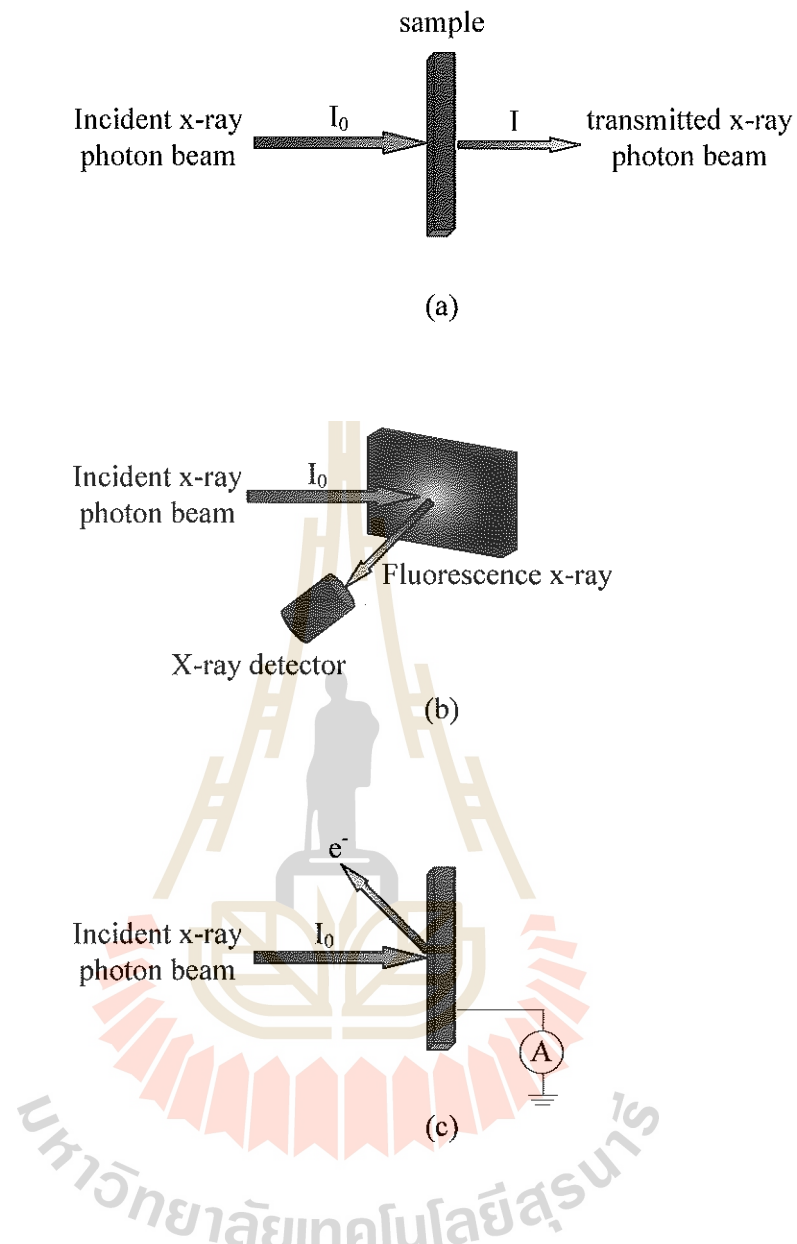
Figure 3.2 The three modes of XAS measurement (a) transmission mode, (b) fluorescence mode and (c) electron yield. (Jutimoosik, 2010)

In transmission mode XAS, after the energy of X-ray photons being changed by X-ray double crystals monochromator, the intensities of incident X-ray photon beam (I_0) and the transmitted X-ray photon beam (I) are measured by ionization chambers as shown in Figure 3.2. In this mode, we make sure the X-ray photon beam is well-

aligned on the sample The experimental set up of XAS experimental station at XAS

beam line, Siam Photon Laboratory, SLRI is shown in Figure 3.4.
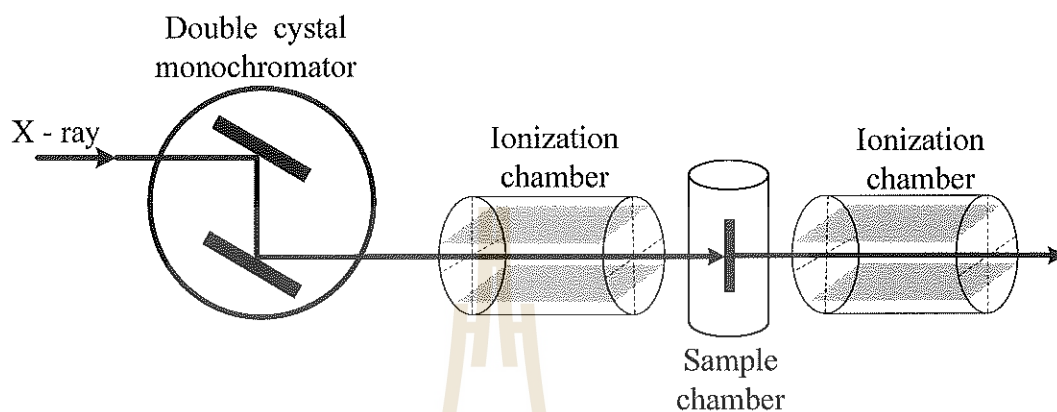
Figure 3.3 Schematic illustration of the experimental setup of transmission-mode

X-ray absorption spectroscopy.
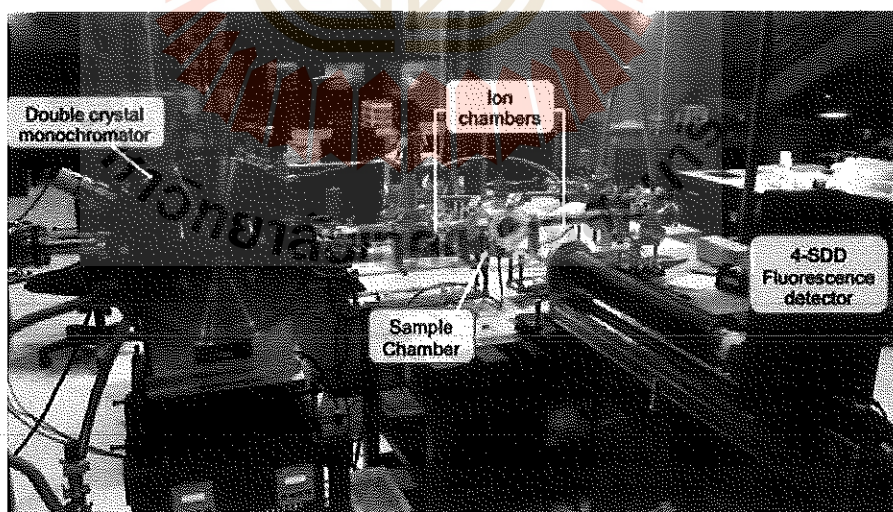
Figure 3.4 XAS experimental set up at the BL 5.2 Siam Photon Laboratory,

Synchrotron Light Research Institute.

Other than the transmission mode, the fluorescence mode and the electron yield are also competent for the measurement of the absorption coefficient. In the X-ray absorption phenomena, where X-ray photon knock out an electron from the inner shell an electron from higher energy level will cascade down to fill in the hole and discharging radiation of energy, the discharged energy X-ray photon will be released as demonstrated in Figure 3.5(a) and the fluorescence X-ray can be detected. In addition, de-excitation can cause the Auger effect, where the electron reduce to lower energy state, a second electron can be excited to the continuum state and perhaps go out from the sample as shown in Figure 3.5(b), and then it can be detected by using the electron-yield XAS detectors.

For fluorescence mode, we measure the intensities of incident X-ray photon beam and the fluorescence X-ray that are emitted following the X-ray absorption. Usually the fluorescence detector is placed at 90° to the incident X-ray photon beam in the horizontal plane, with the sample at an angle (usually 45°) with respect to the beam. Fluctuations in the number of elastically scattered X-ray are a significant source of noise in fluorescence XAS, so the position of the detector is selected to minimize the elastically scattered radiation by exploiting the polarization of the X-ray beam. In case of electron yield, we measure the electrons that are emitted from the surface of the sample. The relative short path length (≈ 1000 Å) makes the technique surface-sensitive, which can be beneficial if one is interested in near-surface phenomena. It also can be beneficial for avoiding "self absorption" effect that occurs in fluorescence mode. However, both modes are instantly equivalent to the absorption ability of the sample. Hence, the three techniques are alterable for the study of the structure of material using the absorption ability of the sample.

E_F

L_3 — — — — $2p_{3/2}^2$
L_2 — — — $2p_{1/2}^2$
L_1 — — $2s^2$
Fluorescent x-ray

K — — — $1s^2$

(a)

Auger electron

E_F

L_3 — — — — $2p_{3/2}^2$
L_2 — — $2p_{1/2}^2$
L_1 — — $2s^2$

K — — $1s^2$

(b)
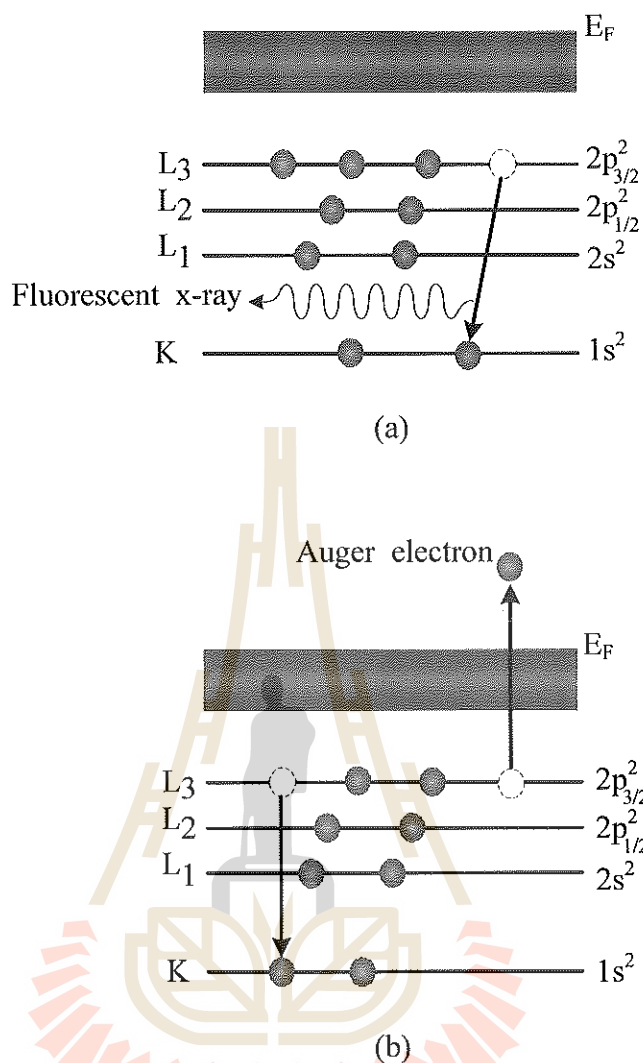
Figure 3.5 The excited state (a) X-ray fluorescence and (b) the Auger effect (Adapted from Jutimoosik, 2010).

3.2.1 In-situ temperature setup

To perform the in-situ XANES measurement under temperature, the small ceramic plate heater was used to demonstrate the effect of temperatures. It was connected to a high voltage power supply and placed between the metal plates in order to increase the temperature. The sample was placed on the metal plates which can obtain effect of temperature as shown in Figures 3.6 and 3.7. The thermocouple

was used to detect temperature on the sample. The BaTiO$_3$ single crystal samples were heated to 50, 100, 120, 130 and 150°C.
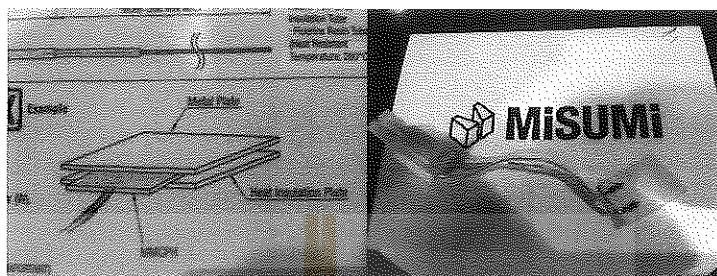
Figure 3.6 Small ceramic plate heater.
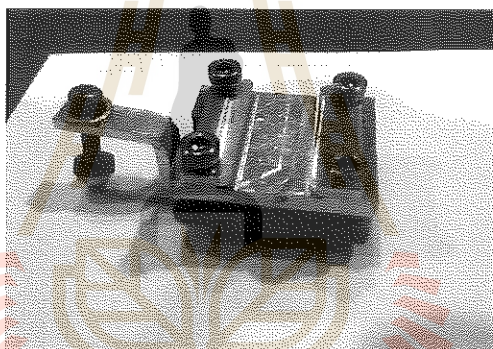
Figure 3.7 Metal plate and heat insulation plate.

3.2.2 In-situ electric field setup

To perform the in-situ XANES measurement under high voltage load, the custom-build sample chamber was designed as shown in Figure 3.8. This special-designed chamber can be subjected to ±1.5 kV and aligned into the incident X-ray beam direction. During the experiment, the sample was installed in the acrylic sample holder. The copper was used as electrical connectors connected to a high voltage power supply. The step DC of 0 V/mm, 85 V/mm, 170V/mm and 255 V/mm with the

current limit of 20 mA was applied to the sample. To prevent the electrical spark, the sample was submerged in silicone oil in the sample holder.
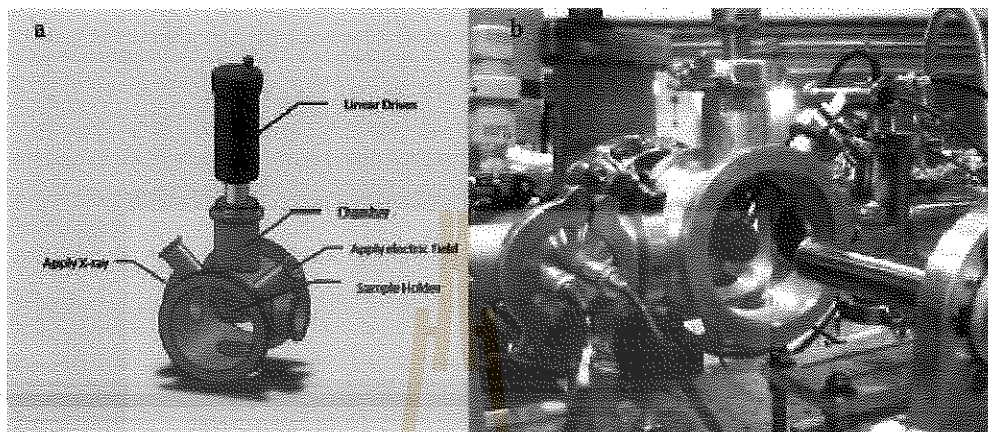
Figure 3.8 Schematic drawing of (a) a sample holder and (b) picture of in-situ X-ray absorption spectroscopy setup (Kempet, 2013).

To detect the change of the atomic structure of BaTiO$_3$ due to the small displacement of Ti atoms, Ti K-edge X-ray absorption spectra were collected at BL5.2. Synchrotron is generated from a bending magnet with a maximum electron beam current of 150 mA and critical energy of 1.2 keV. Incident X-ray s absorption is monochromatized using a Ge(220) fixed exit double-crystal monochromator. The fluorescent X-ray emitted from the sample was recorded by a silicon drift detector (SDD). A titanium metal foil of which K absorption edge is 4966 eV was used for energy calibration with a precision of ±0.2 eV. Spectra were measured over the XANES region from 4946 eV to 5046 eV with an energy step of 0.2 eV and time step of 3 seconds.

3.3 X-ray diffraction (XRD) setup

The Bragg condition can be suitable for each planes of crystal. The half wavelength of the X-ray is smaller than spacing (if $\lambda/2 < d$, then $\sin\theta > 1$, which is impossible). This condition is a limit on how many orders of diffracted waves can be 84 obtained from a given crystal using an X-ray beam of a given wavelength. The crystal patterns, indicated in three dimensions and denoted (*h k l*) are required to describe the order of the diffracted waves or called "the Miller indices", which are used in crystallography, denote the orientation of the reflecting sheets with respect to the unit cell and the path difference in units of wavelength between identical reflecting sheets (Jutimoosik, 2010).

The X-ray diffraction technique is normally carried out by an X-ray diffractometer. The essential components of X-ray diffractometer (Fultz and Howe, 2008) are:

1) A source of X-ray, usually a sealed X-ray tube

2) A goniometer, which provides precise mechanical motions of the tube, specimen and detector

3) An X-ray detector

4) Electronics for counting detector pulses in synchronization with the positions of the goniometer

There are four practical approaches for observing diffractions and making diffraction measurements: Debye-Scherrer Method, Laue Method, Rotating Crystal Method and θ-2θ diffractometer Method. All are designed to ensure that Bragg's law is satisfied. The schematic diagram of θ-2θ X-ray diffractometer used in this work (BRUKER X-ray diffractometer model D5005 equipped with Cu Kα sealed tube,

wave length 1.54 Å) is shown in Figures 3.9. The θ-2θ Diffractometer is used for diffraction measurements of unfixed horizontal sample. For this purpose, this sample will be rotated to θ and X-ray detector moved to 2θ. The diffraction angle followed on Bragg's equation. The one-side weight of the tube stand is compensated by a counter weight. Both tube stand and counter weigh are fixed to the outer ring.
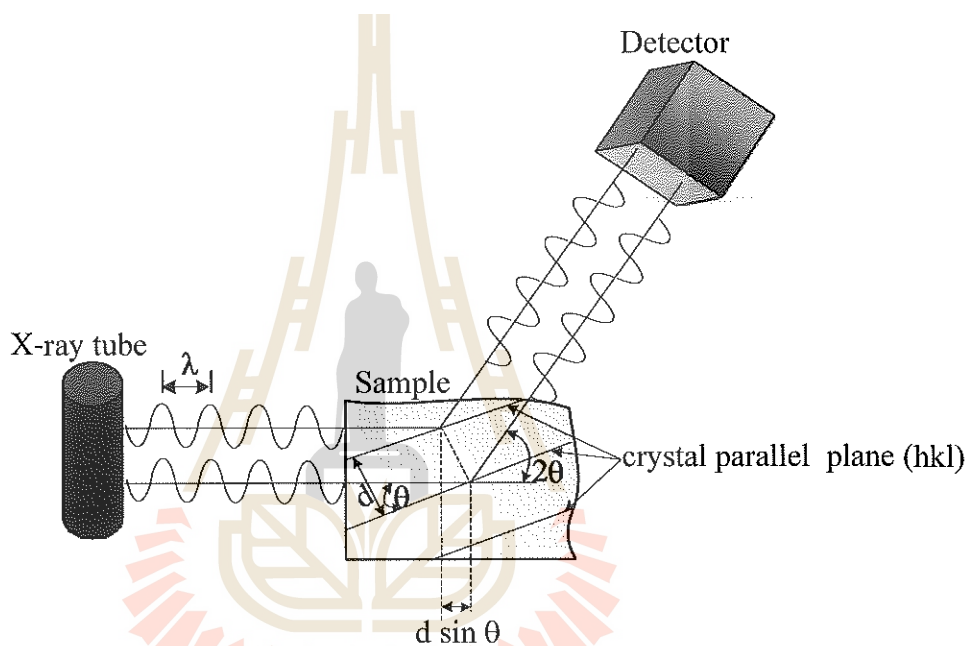
Figure 3.9 Schematic illustration of θ-2θ X-ray diffraction experiment (Jutimoosik, 2010).

3.3.1 X-ray diffraction result

X-ray Diffraction is a one of the standard techniques that can be used to identify the crystal structure of material. Fundamental treatment of X-ray diffraction by crystals is done by considering the interaction of an X-ray plane wave with the electrons of the crystal materials. The wave nature of the X-ray s means that they are reflected by the lattice of the crystal. The XRD results of powders (Lazarevic, 2005) indicate the formation of tetragonal phase of $BaTiO_3$. The appearance of X-ray reflections at $2\Theta = 22.000$, 31.645, 38.955, 44.270 and $56.135°$ is in correlation with JCPDS (31-0174) standards.
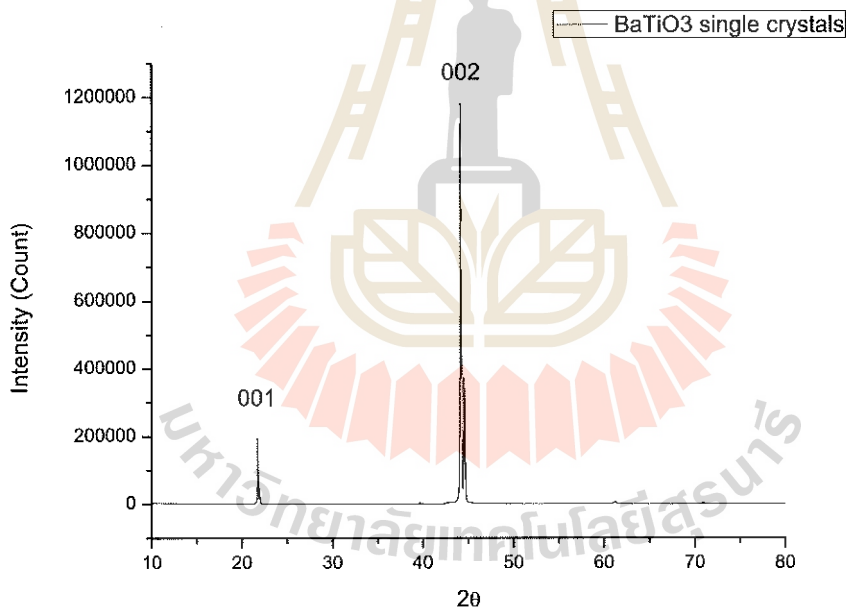
Figure 3.10 X-ray diffraction $BaTiO_3$ single crystal patterns obtained on sample.

From this work, the XRD result shows the formation of tetragonal phase of $BaTiO_3$ single crystal, which is approved by the appearance of X-ray reflections at $2\Theta = 22.000$ and $44.270°$

3.4 Scanning electron microscopy (SEM)

A scanning electron microscope consists of an electron optical column, a vacuum system, electronics, and software. The column is considerably shorter because the only lenses needed are those above the specimen used to focus the electrons into a fine spot on the specimen surface. There are no lenses below the specimen. The SEM model D8 at The Center for Scientific and Technological Equipment Suranaree University of Technology is a type of electron microscope that produces images of a sample by scanning it with a focused beam of electrons. The electrons interact with atoms in the sample, producing various signals that can be detected and that contain information about the sample's surface topography and composition.
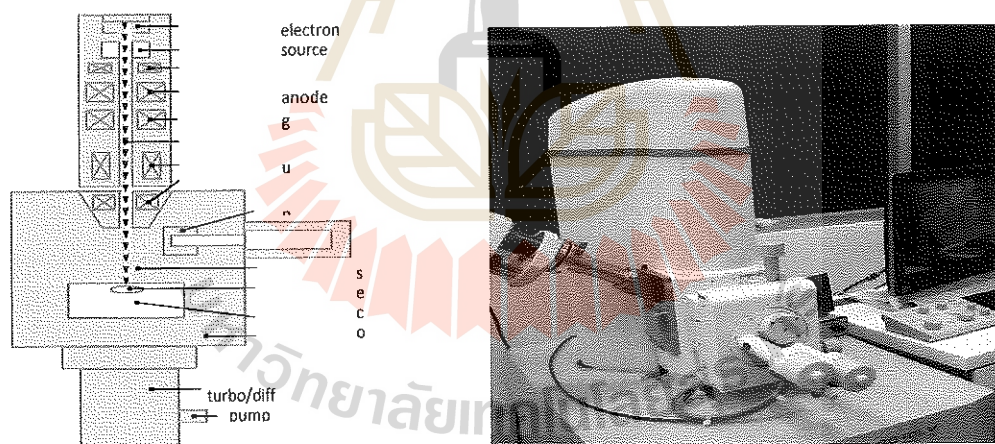
Figure 3.11 SEM model D8 setting up at The Center for Scientific and Technological Equipment, Suranaree University of Technology.

The electron gun at the top of the column produces an electron beam that is focused into a fine spot as small as 1 nm in diameter on the specimen surface. This beam is scanned in a rectangular raster over the specimen and the intensities of

various signals created by interactions between the beam electrons and the specimen are measured and stored in computer memory. The stored values are then mapped as variations in brightness on the image display. The secondary electron (SE) signal is the most frequently used signal. It varies with the topography of the sample surface much like an aerial photograph: edges are bright, recesses are dark. The ratio of the size of the displayed image to the size of the area scanned on the specimen gives the magnification. Increasing the magnification is achieved by reducing the size of the area scanned on the specimen. Because the image in modern SEMs is created in a computer, it can be readily transferred to a hard drive or other medium for long-term storage (Jutimoosik, 2010).

3.4.1 Scanning electron microscope result

SEM is a type of electron microscope that produces images of a sample by scanning it with a focused beam of electrons. The electron beam interacts with the specimen to a depth approximately 1 μm. Complex interactions of the beam electrons with the atoms of the specimen produce wide variety of radiation. The need of understanding of the process of image formation for reliable interpretation of images arises in special situations and mostly in the case of high-magnification imaging. In such case, knowledge of electron optics, beam-specimen interactions, detection, and visualization processes is necessary for successful utilization of the power of the SEM. The SEM image of the surface of $BaTiO_3$ single crystal is shown in Figure 3.12. It shows the morphology in micrometer range without grain boundary was observed, a typical characteristic of a single crystal.

<div align="center">(a)   (b)</div>
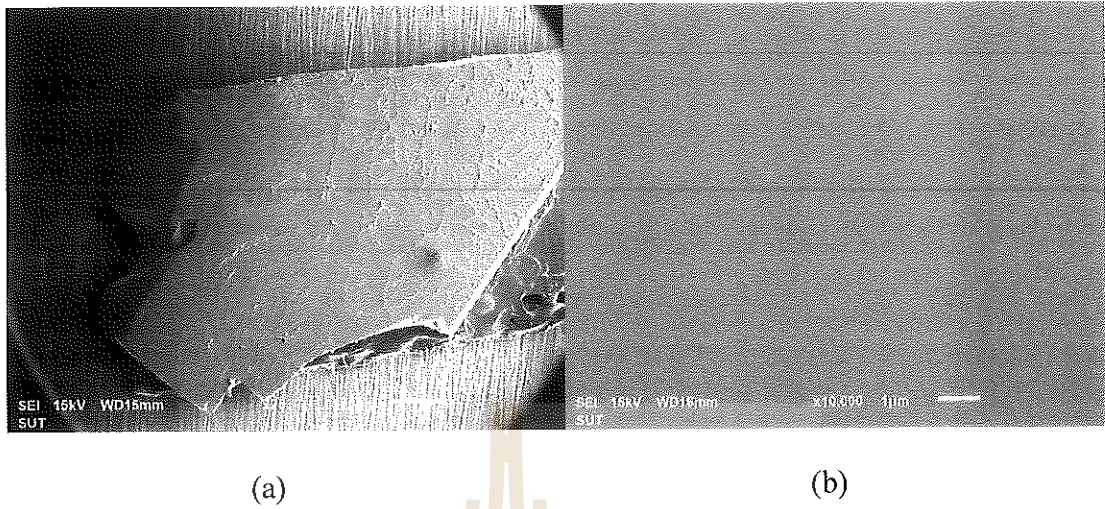
Figure 3.12 (a) SEM micrograph of BaTiO₃ single crystal in range 500 μm. (b) SEM micrograph of BaTiO₃ single crystal in range 1 μm.

CHAPTER IV

RESULTS AND DISCUSSION

In the last chapter the standard characterization study of $BaTiO_3$ single crystal using XRD and SEM show that it is the single crystal. However, the standard characterization cannot reveal the local structure of Ti atom in $BaTiO_3$ single crystal. The synchrotron-based XAS facility was accessible to us through the user beamtime allocated by SLRI. It will be shown in this chapter that XAS is a powerful tool for resolving the local structure surrounding Ti atoms in $BaTiO_3$ single crystal under the effects of temperature and electric field.

4.1 X-ray absorption spectroscopy (XAS) of barium titanate single crystals under the effect of temperature

The XAS measurements were performed in fluorescence mode at the BL-5.2 XAS facility of the Synchrotron Light Research Institute (Public Organization). Figure 4.1 shows the Ti K-edge XANES spectra of the BT single crystal sample at various temperatures. Generally, the XANES spectra show mostly similar features for all temperatures, with small variations observed at several peaks, an indication of changes in the local structure around Ti absorbing atom. XANES measures the excitation of core electrons to unoccupied bound states and is thus used to obtain information about the density of states of unoccupied states and the local arrangement of atoms around the absorbing atoms. The integrated intensity of peak A relates to

electron 1s excite to 3d orbital at 4,970 eV which does not allow by selection rules of dipole transitions. However, the bonding effects of TiO_6 allow the electron 1s excite to 3d orbitals which is described by Ligand field theory (Bootchanont, 2015).
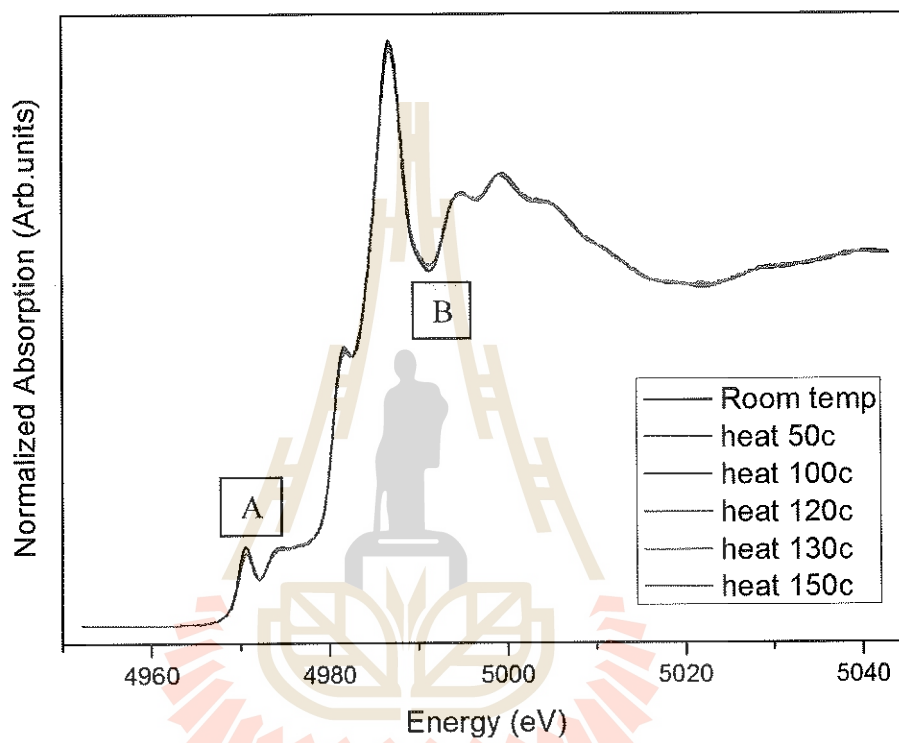
Figure 4.1 The normalized Ti K-edge XANES spectra of $BaTiO_3$ at various temperatures.
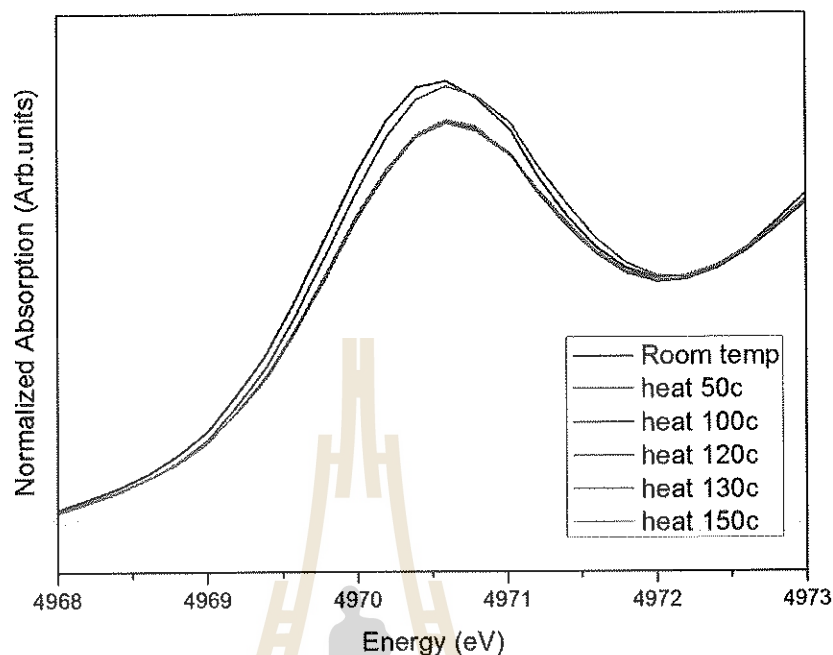
Figure 4.2 Normalized XANES spectra of BaTiO₃ show the intensities of peak A in range of photon energy from 4,968 eV to 4,973 eV at various temperatures.

Figure 4.2 shows the intensity of peak A related to electron $1s$ excite to $3d$ levels. The area of peak A for all spectra is not changed at room temperature and 50°C. However, when temperature is increased to 100°C, the intensity of peak A is decreased. Possiblely, it means that the temperature affects the $3d$ level of Ti atoms and the local structure can be changed from the tetragonal to cubic phase.

The phase transition of BT is obtained from post edge of Ti K-edge XANES spectra, as the post edge is consisting of the spherical wave electron scattering with neighboring atoms around Ti absorbing atom. The nature of BT is a tetragonal perovskite at room temperature. According to Figure 4.3, the post edge of XANES spectra shows slight change with increasing temperature.
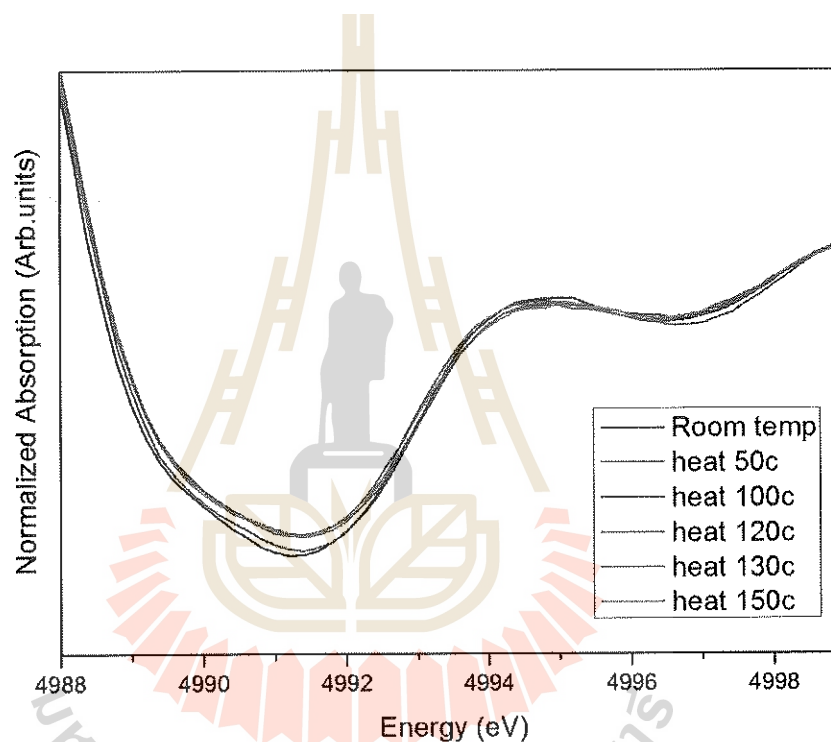
Figure 4.3 The black square in Ti K-edge XANES spectra of BaTiO$_3$ at various temperatures.

As shown more clearly in Figure 4.3, the spectra between 4987 eV to 5002 eV were slightly moved back with increasing temperatures. The starting change was observed when heating from 100°C to 150°C. The tetragonal phase was shown at room temperature and 50°C. When heated to 120°C, the structure of BT can be

transformed to the cubic phase, which is corresponding with the work by Ravel et al., (1998).

Corresponding to the work by Ravel (1998), when the temperature increases to Curie's temperature, the structure of BT can be transformed to cubic phase. Therefore, we assumed that the temperature affects the decrease of c-axis.
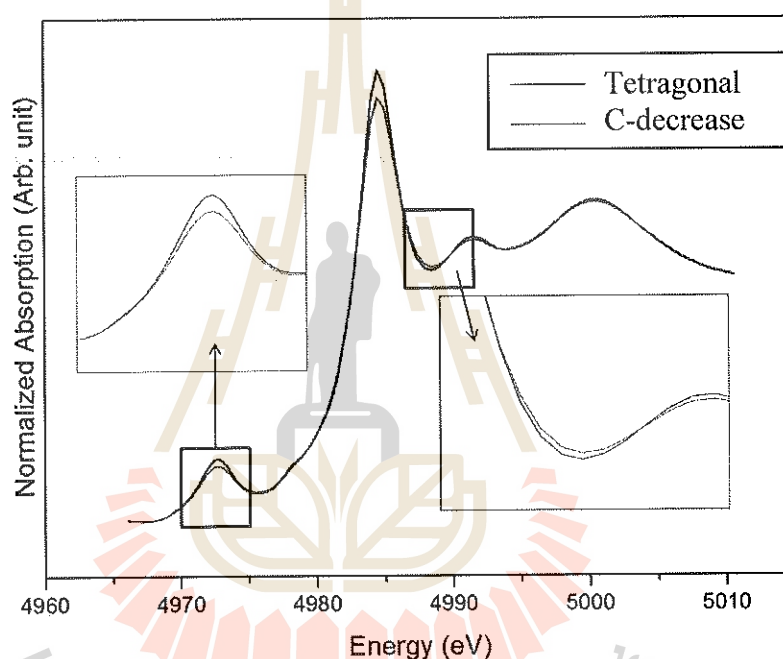
Figure 4.4 Calculated Ti K-edge XANES spectra of tetragonal structure and the c-axis decrease.

The calculated Ti K-edge XANES spectra with tetragonal phase and decreasing c-axis are shown in Figure 4.4. When the C-axis was changed, the differentiation of the XANES spectra is observed. The intensity of peak A and the back scattering are slightly changed.
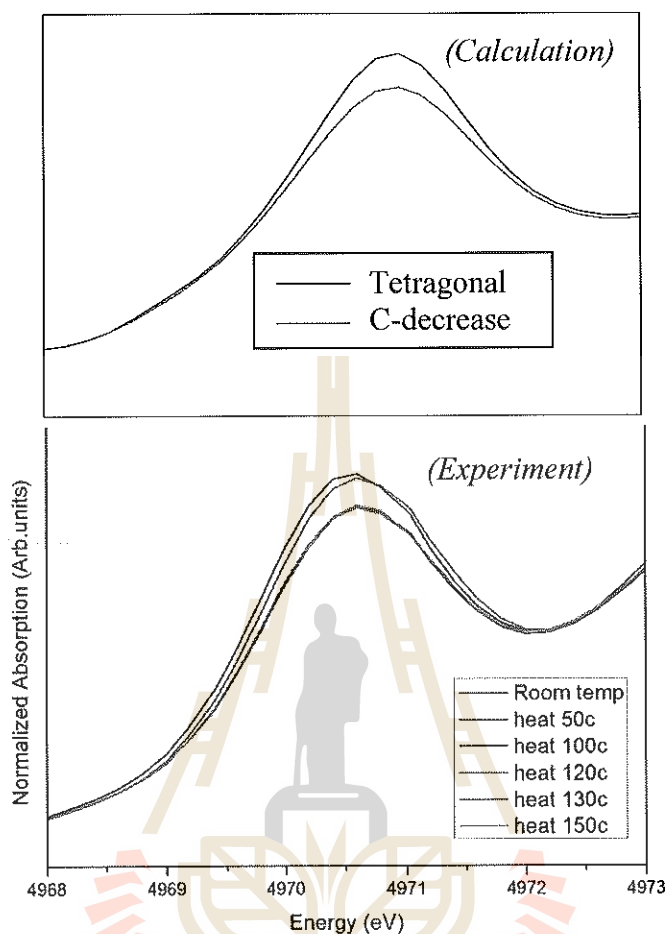
Figure 4.5 The comparisons XANES spectra of BaTiO$_3$ between the experiment and the calculation at the intensity of peak A.

Figure 4.5 shows the comparison of XANES spectra between the experiment and the calculation at the intensity of peak A. Due to the change of c-axis, the intensity of peak A decreases. Then, the back scattering was also increased, as shown in Figure 4.6. Possibly, the temperature affects the change of structure from the tetragonal to cubic phase.
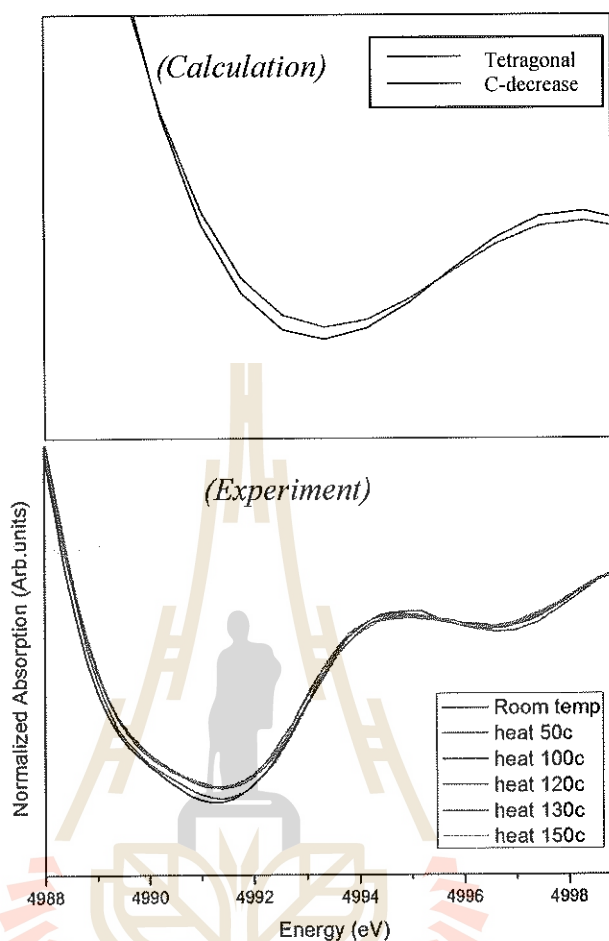
Figure 4.6 The comparisons XANES spectra of BaTiO₃ between the experiment and the calculation at the back scattering.

4.2 X-ray absorption spectroscopy (XAS) of barium titanate single crystals under the effect of electric field

Figure 4.7 shows the normalized Ti K-edge XANES spectra of BaTiO₃ with applied electric field. The intensity change of absorption peaks A and B under the different amplitudes of the applied field was examined. Although the amplitudes of peak A and peak B change slightly during the application of the electric field, this small change is significant for diminutive displacement of Ti atoms. From the

quantitative analysis proposed by RV Vedrinskii et al. (1998) peak A could represent

PEFS formation due to the small displacement of Ti atoms in the perovskite unit cells.
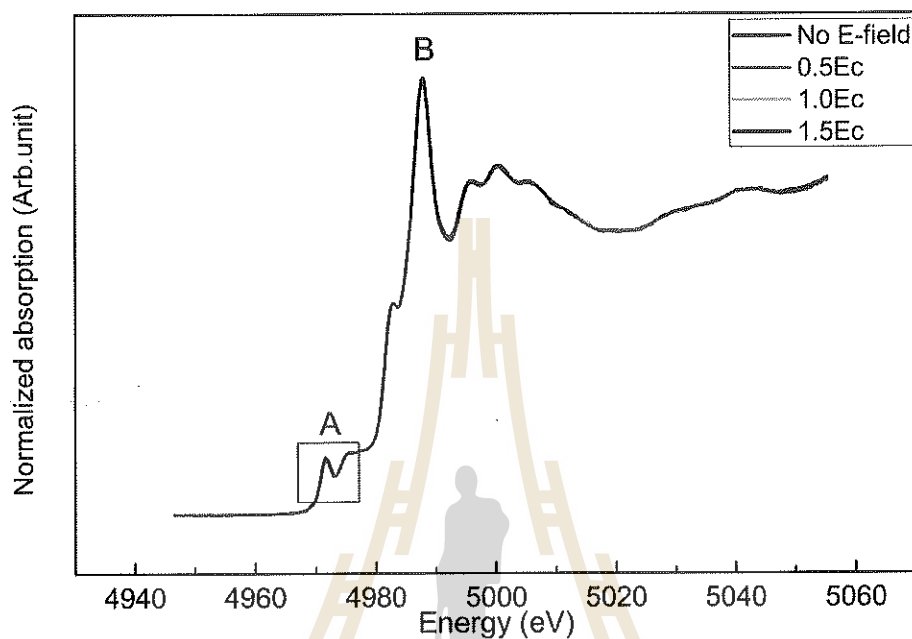
Figure 4.7 The normalized Ti K-edge XANES spectra of BaTiO₃ at without electric field, 0.5Ec, 1.0Ec, 1.5Ec of the applied field.

Figure 4.7 shows the normalized Ti K-edge XANES spectra of BaTiO₃ at without electric field, 0.5Ec, 1.0Ec, 1.5Ec of the applied field. The intensity of peak A which is associated with both the quadrupole and the dipole 1s to 3d transition of Ti and the integral intensity of peak A relates to Ti atom displacement from center. The integral intensity of peak B is a probability of electron 1s excite to the conduction band. The spectrum after peak B is the scattering spherical wave electron with neighboring atom.
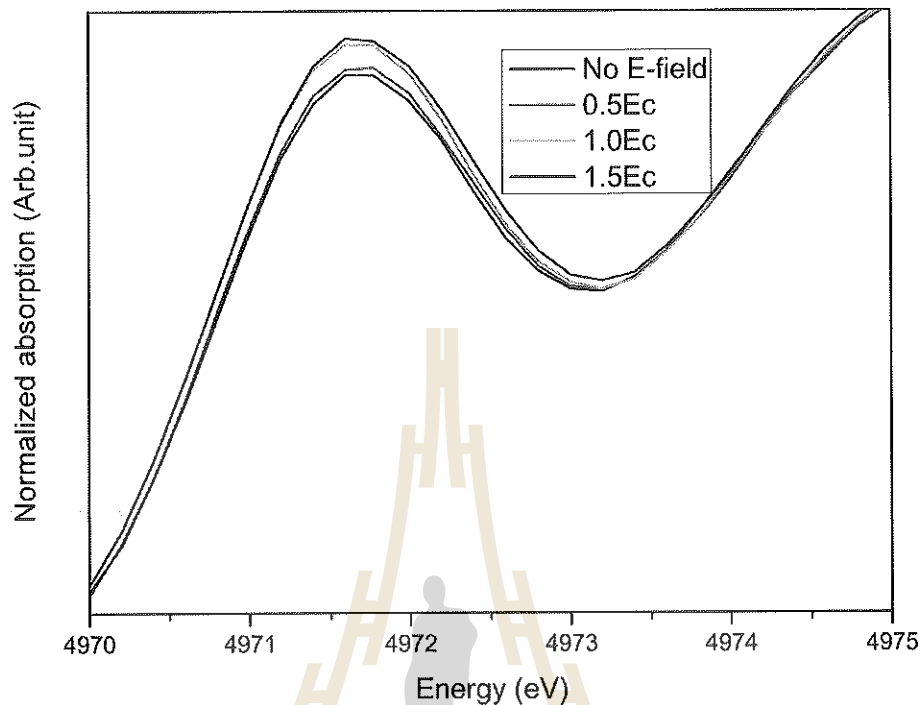
Figure 4.8 The normalized Ti K-edge XANES spectra of BaTiO$_3$ at without electric field, 0.5Ec, 1.0Ec, 1.5Ec of the applied field at the intensity of peak A.

The intensity of peak A relates to the Ti displacement off center of BaTiO$_3$ perovskite structure. The intensity of peak A increases when applying electric field. It means the increasing of Ti displacement, so the polarization increases too.

The displcement of Ti atom move from the center can be calculated by Vedrinskii method. The integrated intensity of Ti K pre-edge, which is associated with both the quadrupole and the dipole 1s $\longrightarrow$ 3d transition of Ti, reflects the 3d-4p hybridization for Ti. This hybridization results from displacement of the Ti atom from centro-symmetric position within the oxygen octahedron. Vedrinskii et al. (1998). have shown that a contribution to the area under peak X is given by

$$A = \frac{\gamma s}{3} \, d_s^2$$

In this equation, d_s is the mean-square displacement of Ti atom from center and a is the average displacement of the oxygen octahedral and A is a peak area. An experimental determination of the constant γs by Ravel resulted in values of 11.2 eV/Å^2 for BaTiO$_3$. From this equation, we calculate area under peak A in order to investigate the Ti atom displacement, as shown in Table 4.1.

Table 4.1 The result of calculated area under pre-edge peak and Ti atom displacement.

Applied Electric field	Area under the peak (eV (a.u.))	d_s (Å)
Without electric field	0.141	0.1943
0.5Ec	0.145	0.1971
1.0Ec	0.152	0.2018
1.5Ec	0.154	0.2031
1.0Ec return	0.153	0.2011
0.5Ec return	0.146	0.1984
Return to zero field	0.143	0.1964
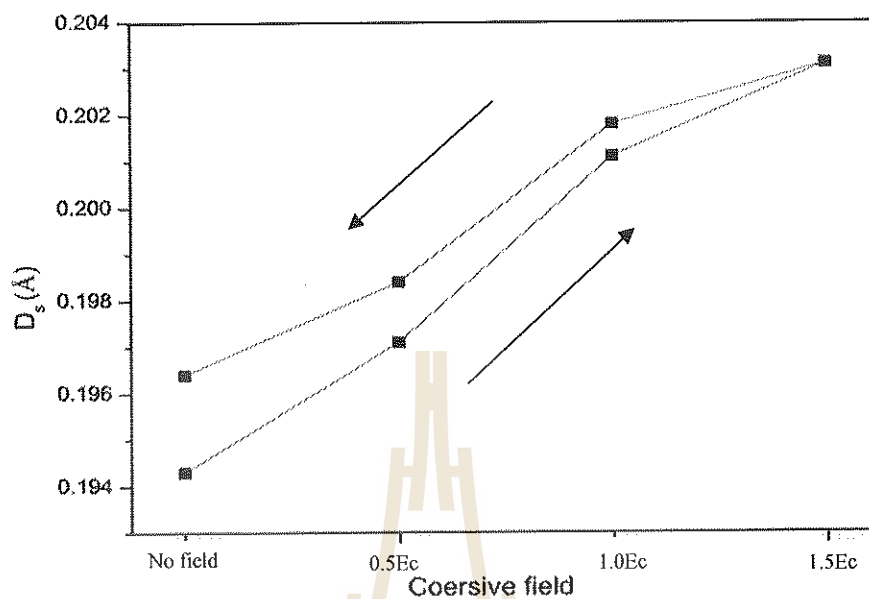
Figure 4.9 The Ti-off center in perovskite structure with applied electric fields.

Figure 4.9 shows the Ti-off center in perovskite structure with applied electric fields. When applying field on the sample, the Ti-off center is increasing until 1.5Ec or saturation. After then, the decrease in the applied fields, the Ti-off center will decrease again, but the value will not be equal to the first cycle of the applied field. Thus, at the applied field =0, the Ti-off center is a little more than the original value. It means that it still has the remnant polarization. This result is in good agreement and corresponding with dielectric behavior (Lazarevic, 2005).
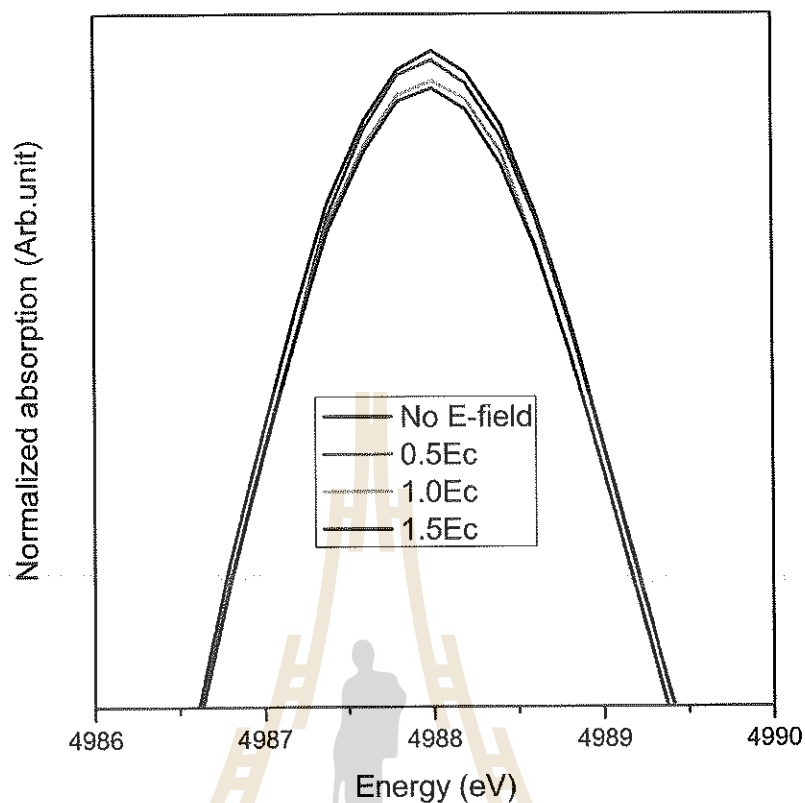
Figure 4.10 The normalized Ti K-edge XANES spectra of BaTiO₃ at without electric field, 0.5Ec, 1.0Ec, 1.5Ec of the applied field at the intensity of peak B.

Effect of applied electric field leads to the integral intensity of peak B decreases. As mentioned previously, the probability of electron 1s excite to the conduction band affects to the integral intensity of peak B. Possibly, when applying electric field, the absorbance of external energy occurs, thus some electrons in valence band can be excited to conduction band more easily. Then, when the electron 1s has sufficient energy, it can be excited to conduction band. Therefore, the probability of electron 1s excited to the conduction band is reduced.
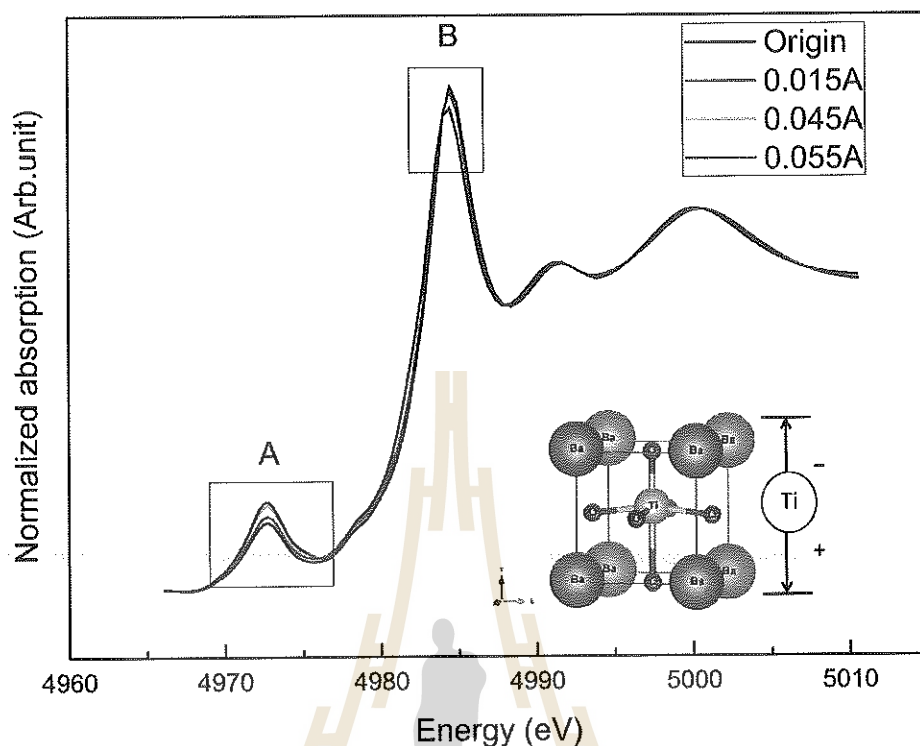
Figure 4.11 Calculated Ti K-edge XANES spectra at 0 Å, 0.015 Å, 0.045 Å and 0.55 Å of Ti off-center displacements by using FEFF8.2 software.

To support the experimental results, the Ti K-edge XANES spectra of $BaTiO_3$ with tetragonal phase is calculated by using FEFF 8.2 program. The calculated XANES spectra under different Ti off-center positions which are in the range of 0 Å, 0.015 Å, 0.045 Å and 0.055 Å are shown in Figure 4.11. The experimental results show that the intensity peak A increases and the intensity of peak B decreases. It is seen from the calculation that the Ti atom displacement affects the intensity of peak A and peak B.
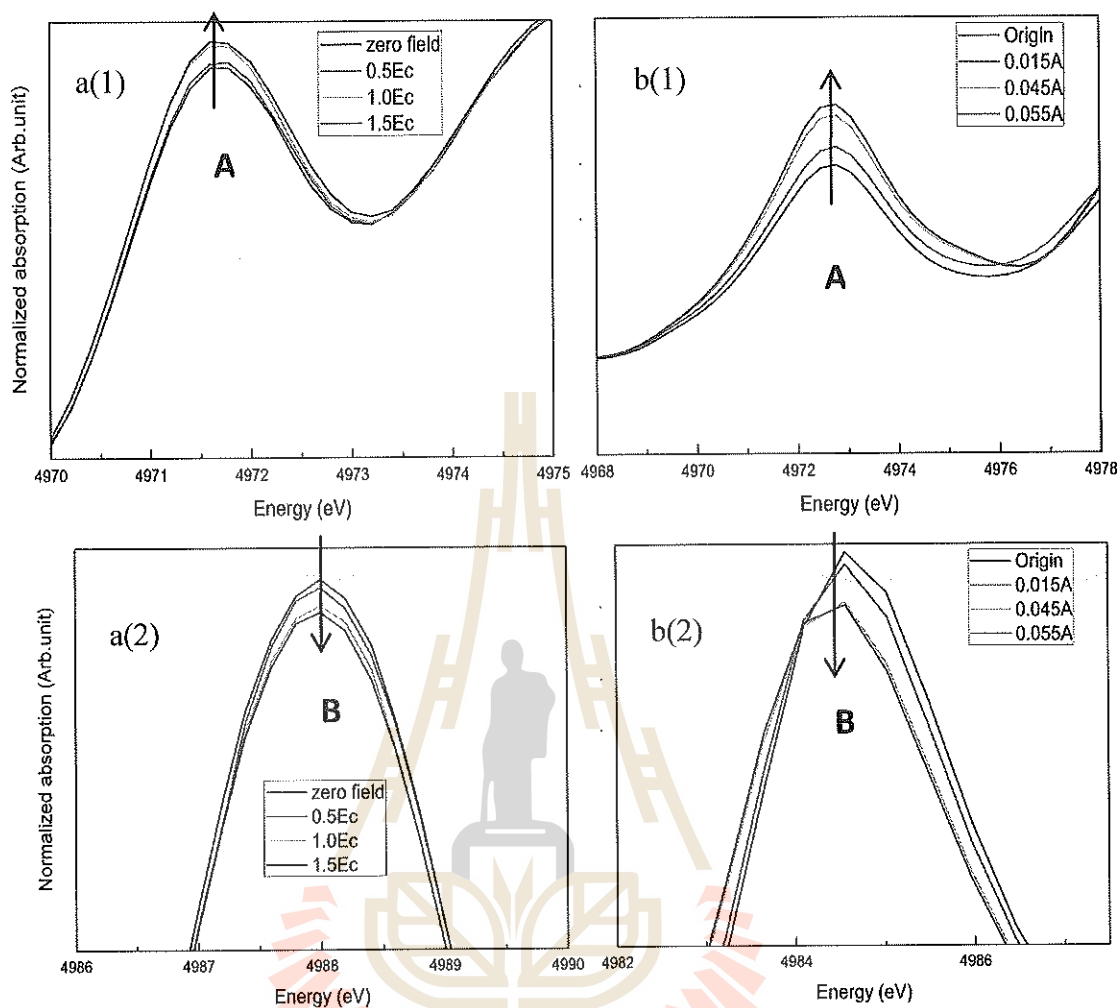
Figure 4.12 The PEFS of Ti K-edge X-ray absorption obtained from (a) experiment at different applied fields and (b) calculations at different Ti displacements.

The calculated spectra demonstrate the change of peak A intensity due to small displacement of Ti atoms. The calculated intensity increases when the Ti atoms shift to a positive position. This simulation result is overall in good agreement with the experiment. Similarly, the intensity of peak B obtained from the calculation also drops if the field is on. It can be seen that the change of the experiment results are overall in good agreement with the calculations.

4.2.1 EXAFS results

To process and enhance the EXAFS with the high k region, the plot $k2X(k)$ is considered and windowed using a Hanning window $W(k)$. The EXAFS spectra were processed and information on local structure of Ti atom was obtained via fitting with perovskite models of $BaTiO_3$ in ARTEMIS program. In this work, the Ti K-edge EXAFS spectra can only be obtained up to photon energy of 250 eV above the absorption edge, due to the presence of Ba L_3-edge. Therefore, EXAFS spectral fitting can only be performed up to the first shell-oxygen octahedral. The range of Fourier transform of k space was limited to about k=6.5, after which the signal became very noisy, as shown in Figure 4.13. The Fourier transform in R space showed that the features change when applied electric field (Figure 4.15), where the Ti-atom move off center. This result can be confirmed by the XANES and EXAFS.
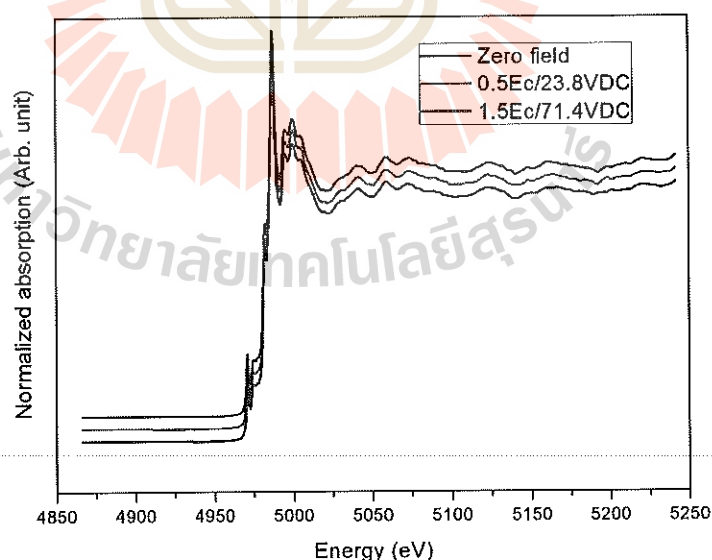
Figure 4.13 The normalized EXAFS signal of $BaTiO_3$ single crystal were applied electric field.
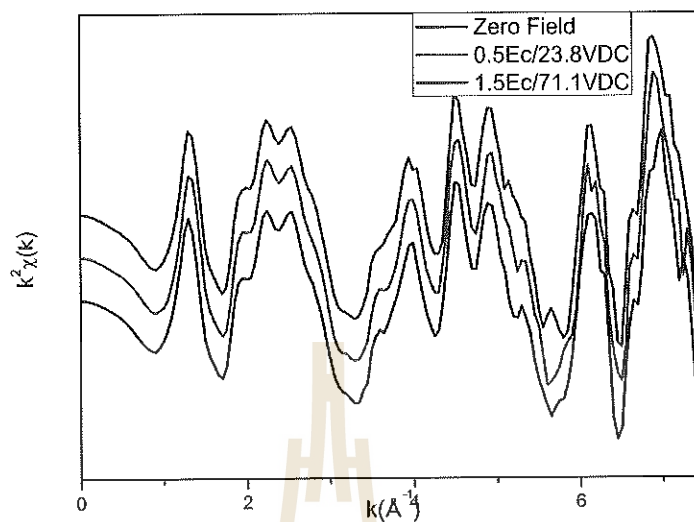
Figure 4.14 The EXAFS Fourier transform in k-space of BaTiO₃ single crystal were applied electric field.
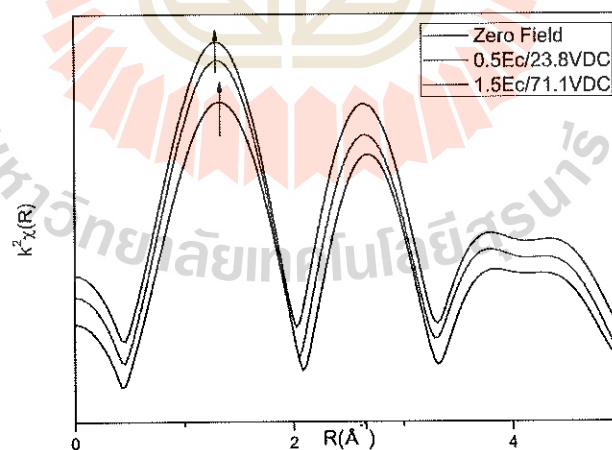
Figure 4.15 The EXAFS Fourier transform in R-space of BaTiO₃ single crystal with applied electric field.

Table 4.2 The structural parameters coordination numbers N, interatomic distances R and DW factors σ^2 obtained by fitting the EXAFS data for the $BaTiO_3$ single crystal under applied electric field.

Sample	Shell	N	R (Å)	σ^2
BaTiO₃ without electric field	Ti-O1	1	1.54±0.006	0.003
	Ti-O2	4	1.83±0.0005	0.003
	Ti-O3	1	2.055±0.005	0.003
BaTiO₃ applied electric field 0.5Ec	Ti-O1	1	1.52±0.008	0.003
	Ti-O2	4	1.84±0.007	0.003
	Ti-O3	1	2.08±0.006	0.003
BaTiO₃ applied electric field 1.5Ec	Ti-O1	1	1.50±0.007	0.008
	Ti-O2	4	1.85±0.001	0.008
	Ti-O3	1	2.11±0.006	0.008

The refined structural parameters are summarized in Table 4.2, showing coordination numbers N, the bond length of Ti absorbing atoms within oxygen octahedral with 8-fold barium atoms and the Debye-Waller (DW) factor σ^2. It is observed that with increasing electric field in $BaTiO_3$ system, the applied electric field affects the Ti displacement.

CHAPTER V

CONCLUSIONS

In this work, XAS technique was employed to investigate the local structure of $BaTiO_3$ single crystals. The synchrotron XANES and EXAFS measurements were performed at the X-ray absorption spectroscopy beamlines (BL-5.2) of the Synchrotron Light Research Institute (SLRI, Thailand) for understanding the phase transition and the Ti atom distortion of perovskite structure.

$BaTiO_3$ single crystals used in this work were grown by a Remeika process. The global structural information was examined by X-ray Diffraction (XRD) technique and standard characterization technique such as SEM was used for surface analysis. The results of XRD and SEM showed that the formation of tetragonal phase of $BaTiO_3$ single crystal and the morphology in micrometer range without grain boundary was observed, a typical characteristic of a single crystal.

The effect of temperature results showed the local structure of $BaTiO_3$ single crystals was be transformed to cubic phase around the Curie's temperature. Under an application of electric field, the experimental XAS results, both in XANES and EXAFS regions, showed that the Ti atom among O octahedral was distorted by applied field. The XAS experiment results can be confirmed by the FEFF8.2 calculation.
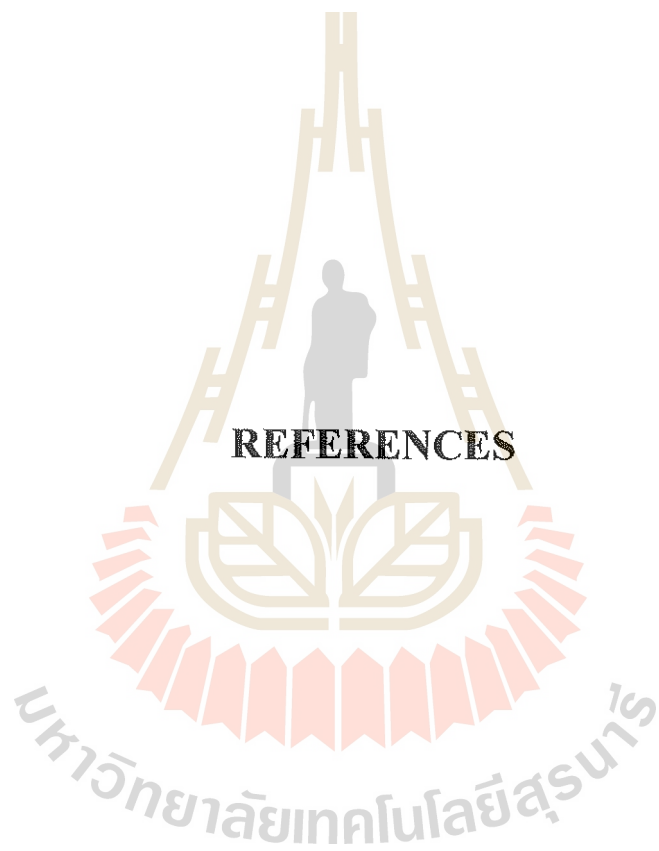
REFERENCES

REFERENCES

Ankudinov, A. L., Ravel, B., Rehr, J. J., and Conradsan, S. D. (1998). Real-space multiple-scattering calculation and interpretation of x-ray-absorption near-edge structure. **Physical Review. B.** 58: 7565.

Bootchanont, A. (2015). Local structure and dielectric properties of barium titanate based relaxer ferroelectrics. **Suranaree University of Technology Ph.D. Thesis.** 1: 27.

Brandon, D. G., and Kaplan, W. D. (1999). Microstructural characterization of materials. Chichester: Wiley.

Filho, F. M. (2006). Ferroelectricidade em ceramicas policristalinas (perovskitas) ABO_3 **Seminario.** Araraquara.

Fong, C. Y., Weber, W., and Phillips, J. C. (1976). Violation of Vegard's law in covalent semiconductor alloys. **Physics Review. B.** 14(2): 5387-5391.

Guinier, A. (1994). **X-ray diffraction: In crystals, imperfect crystals, and amorphous bodies.** New York: W. H. Freeman.

Haertling, G. H. (1999). Multifunctional polycrystalline ferroelectric materials: processing and properties. **Journal of American Ceramic Society.** 82: 797.

Harvey, D. (2000). **Modern analytical chemistry.** New York: McGraw-Hill.

Jona, F., and Shirane, G. (1993). Environmental friendly lead-free piezoelectric materials. Ferroelectric crystals, **Dover Publications.** INC., New York.

Jutimoosik, J. (2010). **Local Structure of Magnesium Zinc Oxide Nanocrystals.** M.S. thesis, Suranaree University of Technology, Nakhon Ratchasima.

Kawai, J. (2000). **Absorpyion techniques in x-ray spectrometry, Encyclopedia of analytical chemistry**. New York: Wiley.

Kempet, W., Marungsri, B., Yimniran, R., Klysubun, W., and Pojprapai, S. (2013). Investigation of Unit Cell Distortion in PZT. **Ferroelectrics**. 453: 1, 106-112.

Koelzynski, A., and Tkacz-Smiech, K. (2005). History and Challenges of Barium Titanate. **Ferroelectrics**. 314: 123.

Koningsberger, D. C., and Prins, R. (1998). **X-ray Absorption: Principles, Applications, Techniques of EXAFS, SEXAFS and XANES**. New York: Wiley.

Lazarevic, Z., Stojanovic, B. D., and Varela, J. A. (2005). An Approach to Analyzing Synthesis, Structure and Properties of Bismuth Titanate Ceramics. **Science Sintering**. 37: 199.

Maiti, T., Guo, R., and Bhalla, A. S. (2008). Structure-Property Phase Diagram of $BaZr_xTi_{1-x}O_3$ System. **Journal of the American Ceramic Society**. 91: 1769.

Ravel, B., Stern, E. A., Vedrinskii, R. I., and Kraizman, V. (1998). Local structure and the phase transitions of $BaTiO_3$. **Ferroelectrics**. 206: 407-430.

Rehr, J. J., and Albers, R. C. (2000). Theoretical approaches to x-ray absorption fine structure. **Reviews of Modern Physics**. 72: 621.

Rouessac, F., and Rouessac, A. (2004). **Chemical analysis: Modern instrumentation methods and techniques**. Chichester: Wiley.

Sabolsky, E., Trolier-McKinstry, S., and Messing, Gary L. (2001). Phenomenologically derived electric field-temperature phase diagrams. **Applied Physics Letter**. 78: 2551.

Shieh, J., Yeh, J. H., Shu, Y. C., and Yen, J. H. (2009). Hysteresis behaviors of barium titanate single crystals based on the operation of multiple 90° switching systems. **Materials Science and Engineering B**. 161: 50-54.

Vedrinskii, R. V., Kraizman, V. L., Novakovich, A. A., Demekhin P. V., and Urazhdin, S. V. (1998). Pre-edge fine structure of the 3d atom K X-ray absorption spectra and quantitative atomic structure determinations for ferroelectric perovskite structure crystals. **Journal of Physics Condensed Matter**. 10: 9561.

Vijatović, M. M., Bobić, J. D., and Stojanović, B. D. (2008). History and challenges of barium titanate: Part I. **Science of Sintering**. 155-165.

Wang, J. J., Wu, P. P., Ma, X. Q., and Chen, L. Q. (2010). Temperature-pressure phase diagram and ferroelectric properties of BaTiO$_3$ single crystal based on a modified Landau potential. **Journal of Aplied Physics**. 114105.

Wei, X., and Yao, X. (2007). Preparation, structure and dielectric property of barium stannate titanate ceramics. **Materials Science and Engineering B**. 137: 184.

Yoon, S., and Baik, S. (2006). Formation mechanisms of tetragonal barium titanate nanoparticles in alkoxide–hydroxide sol-precipitation synthesis. **Journal of American Ceramic Society**. 89: 1816-1821.

APPENDIX

Atom input of Tetragonal structure

```
title BaTiO3
Space P 4 m m
a=3.992 C=4.034
alpha=90.000 beta=90.000 gamma=90.000
core=Ti
rmax=8
atom
! At.type  x          y         z
      Ba 0.0000   0.0000   0.0202
      O  0.0000   0.5000   0.4920
      O  0.5000   0.0000   0.4920
      O  0.5000   0.5000   0.9780
      Ti 0.5000   0.5000   0.5389
```

FEFF in put of Tetragonal structure

```
* This feff.inp file generated by ATOMS, version 2.50
 * ATOMS written by and copyright (c) Bruce Ravel, 1992-1999

 * -- * -- * -- * -- * -- * -- * -- * -- * -- * -- * -- * -- *
-- * -- *
 *          total mu =       1862.2 cm^-1, delta mu =       750.8
cm^-1
 *          specific gravity =  6.852, cluster contains   147
atoms.
 * -- * -- * -- * -- * -- * -- * -- * -- * -- * -- * -- * -- *
-- * -- *
 *          mcmaster corrections:  0.00093 ang^2 and   0.165E-05
ang^4
 * -- * -- * -- * -- * -- * -- * -- * -- * -- * -- * -- * -- *
-- * -- *

 TITLE    BaTiO3

 EDGE     K
 S02      1.0

 *          pot    xsph   fms    paths  genfmt ff2chi
 CONTROL  1      1      1      1      1      1
 PRINT    1      0      0      0      0      0

 *          r_scf  [ l_scf n_scf ca ]
 SCF      3.00000   0       30      0.1

 *          ixc  [ Vr  Vi ]
 EXCHANGE 0       1    0.3

 *EXAFS
 *RPATH    7.79385

 *          kmax [ delta_k delta_e ]
 XANES    9.5      0.03      0.3
```

```
*            r_fms       [ l_fms ]
FMS       6.0000000       0
*
RPATH     0.10000
*         emin   emax   resolution
*LDOS      -20    20    0.1

POTENTIALS
*   ipot   z [ label   l_scmt   l_fms   stoichiometry ]
     0    22     Ti      -1       -1          0
     1     8     O       -1       -1          5
     2    56     Ba      -1       -1          1
     3    22     Ti      -1       -1          1

 ATOMS
   0.00000      0.00000      0.00000      0    Ti
0.00000
   0.00000      0.00000      1.77133      1    O
1.77133
  -1.99600      0.00000     -0.18919      1    O
2.00495
   1.99600      0.00000     -0.18919      1    O
2.00495
   0.00000     -1.99600     -0.18919      1    O
2.00495
   0.00000      1.99600     -0.18919      1    O
2.00495
   0.00000      0.00000     -2.26267      1    O
2.26267
  -1.99600      1.99600      1.94156      2    Ba
3.42603
   1.99600      1.99600      1.94156      2    Ba
3.42603
  -1.99600     -1.99600      1.94156      2    Ba
3.42603
   1.99600     -1.99600      1.94156      2    Ba
3.42603
   1.99600      1.99600     -2.09244      2    Ba
3.51373
  -1.99600     -1.99600     -2.09244      2    Ba
3.51373
   1.99600     -1.99600     -2.09244      2    Ba
3.51373
  -1.99600      1.99600     -2.09244      2    Ba
3.51373
   0.00000      3.99200      0.00000      3    Ti
3.99200
   0.00000     -3.99200      0.00000      3    Ti
3.99200
  -3.99200      0.00000      0.00000      3    Ti
3.99200
   3.99200      0.00000      0.00000      3    Ti
3.99200
```

0.00000	0.00000	-4.03400	3	Ti
4.03400				
0.00000	0.00000	4.03400	3	Ti
4.03400				
-1.99600	0.00000	3.84481	1	O
4.33204				
0.00000	-1.99600	3.84481	1	O
4.33204				
0.00000	1.99600	3.84481	1	O
4.33204				
1.99600	0.00000	3.84481	1	O
4.33204				
0.00000	3.99200	1.77133	1	O
4.36734				
0.00000	-3.99200	1.77133	1	O
4.36734				
-3.99200	0.00000	1.77133	1	O
4.36734				
3.99200	0.00000	1.77133	1	O
4.36734				
-3.99200	1.99600	-0.18919	1	O
4.46720				
-1.99600	3.99200	-0.18919	1	O
4.46720				
3.99200	1.99600	-0.18919	1	O
4.46720				
-3.99200	-1.99600	-0.18919	1	O
4.46720				
1.99600	3.99200	-0.18919	1	O
4.46720				
3.99200	-1.99600	-0.18919	1	O
4.46720				
1.99600	-3.99200	-0.18919	1	O
4.46720				
-1.99600	-3.99200	-0.18919	1	O
4.46720				
0.00000	3.99200	-2.26267	1	O
4.58865				
-3.99200	0.00000	-2.26267	1	O
4.58865				
3.99200	0.00000	-2.26267	1	O
4.58865				
0.00000	-3.99200	-2.26267	1	O
4.58865				
0.00000	1.99600	-4.22319	1	O
4.67112				
1.99600	0.00000	-4.22319	1	O
4.67112				
-1.99600	0.00000	-4.22319	1	O
4.67112				
0.00000	-1.99600	-4.22319	1	O
4.67112				

-3.99200	3.99200	0.00000	3	Ti
5.64554				
-3.99200	-3.99200	0.00000	3	Ti
5.64554				
3.99200	-3.99200	0.00000	3	Ti
5.64554				
3.99200	3.99200	0.00000	3	Ti
5.64554				
3.99200	0.00000	4.03400	3	Ti
5.67532				
0.00000	3.99200	4.03400	3	Ti
5.67532				
3.99200	0.00000	-4.03400	3	Ti
5.67532				
0.00000	-3.99200	4.03400	3	Ti
5.67532				
-3.99200	0.00000	4.03400	3	Ti
5.67532				
0.00000	-3.99200	-4.03400	3	Ti
5.67532				
-3.99200	0.00000	-4.03400	3	Ti
5.67532				
0.00000	3.99200	-4.03400	3	Ti
5.67532				
0.00000	0.00000	5.80533	1	O
5.80533				
-1.99600	3.99200	3.84481	1	O
5.89089				
-1.99600	-3.99200	3.84481	1	O
5.89089				
3.99200	1.99600	3.84481	1	O
5.89089				
1.99600	3.99200	3.84481	1	O
5.89089				
-3.99200	1.99600	3.84481	1	O
5.89089				
1.99600	-3.99200	3.84481	1	O
5.89089				
3.99200	-1.99600	3.84481	1	O
5.89089				
-3.99200	-1.99600	3.84481	1	O
5.89089				
-3.99200	3.99200	1.77133	1	O
5.91690				
3.99200	-3.99200	1.77133	1	O
5.91690				
-3.99200	-3.99200	1.77133	1	O
5.91690				
3.99200	3.99200	1.77133	1	O
5.91690				
0.00000	-5.98800	-0.18919	1	O
5.99099				

5.98800	0.00000	-0.18919	1	O	5.99099
-5.98800	0.00000	-0.18919	1	O	5.99099
0.00000	5.98800	-0.18919	1	O	5.99099
-3.99200	3.99200	-2.26267	1	O	6.08209
-3.99200	-3.99200	-2.26267	1	O	6.08209
3.99200	-3.99200	-2.26267	1	O	6.08209
3.99200	3.99200	-2.26267	1	O	6.08209
-1.99600	3.99200	-4.22319	1	O	6.14455
1.99600	3.99200	-4.22319	1	O	6.14455
3.99200	-1.99600	-4.22319	1	O	6.14455
1.99600	-3.99200	-4.22319	1	O	6.14455
-3.99200	-1.99600	-4.22319	1	O	6.14455
-1.99600	-3.99200	-4.22319	1	O	6.14455
-3.99200	1.99600	-4.22319	1	O	6.14455
3.99200	1.99600	-4.22319	1	O	6.14455
0.00000	0.00000	-6.29667	1	O	6.29667
5.98800	-1.99600	1.94156	2	Ba	6.60377
-5.98800	1.99600	1.94156	2	Ba	6.60377
-5.98800	-1.99600	1.94156	2	Ba	6.60377
1.99600	-5.98800	1.94156	2	Ba	6.60377
1.99600	5.98800	1.94156	2	Ba	6.60377
5.98800	1.99600	1.94156	2	Ba	6.60377
-1.99600	-5.98800	1.94156	2	Ba	6.60377
-1.99600	5.98800	1.94156	2	Ba	6.60377
1.99600	1.99600	5.97556	2	Ba	6.60874
-1.99600	-1.99600	5.97556	2	Ba	6.60874

1.99600	-1.99600	5.97556	2	Ba
6.60874				
-1.99600	1.99600	5.97556	2	Ba
6.60874				
-1.99600	-5.98800	-2.09244	2	Ba
6.64970				
5.98800	1.99600	-2.09244	2	Ba
6.64970				
5.98800	-1.99600	-2.09244	2	Ba
6.64970				
1.99600	5.98800	-2.09244	2	Ba
6.64970				
-5.98800	-1.99600	-2.09244	2	Ba
6.64970				
-5.98800	1.99600	-2.09244	2	Ba
6.64970				
1.99600	-5.98800	-2.09244	2	Ba
6.64970				
-1.99600	5.98800	-2.09244	2	Ba
6.64970				
1.99600	1.99600	-6.12644	2	Ba
6.74546				
-1.99600	-1.99600	-6.12644	2	Ba
6.74546				
1.99600	-1.99600	-6.12644	2	Ba
6.74546				
-1.99600	1.99600	-6.12644	2	Ba
6.74546				
3.99200	3.99200	-4.03400	3	Ti
6.93868				
-3.99200	3.99200	4.03400	3	Ti
6.93868				
3.99200	-3.99200	4.03400	3	Ti
6.93868				
-3.99200	3.99200	-4.03400	3	Ti
6.93868				
3.99200	-3.99200	-4.03400	3	Ti
6.93868				
-3.99200	-3.99200	-4.03400	3	Ti
6.93868				
-3.99200	-3.99200	4.03400	3	Ti
6.93868				
3.99200	3.99200	4.03400	3	Ti
6.93868				
3.99200	0.00000	5.80533	1	O
7.04542				
-3.99200	0.00000	5.80533	1	O
7.04542				
0.00000	-3.99200	5.80533	1	O
7.04542				
0.00000	3.99200	5.80533	1	O
7.04542				

```
    -5.98800      0.00000      3.84481      1    O
 7.11609
     5.98800      0.00000      3.84481      1    O
 7.11609
     0.00000     -5.98800      3.84481      1    O
 7.11609
     0.00000      5.98800      3.84481      1    O
 7.11609
     5.98800      3.99200     -0.18919      1    O
 7.19917
    -3.99200      5.98800     -0.18919      1    O
 7.19917
    -3.99200     -5.98800     -0.18919      1    O
 7.19917
     5.98800     -3.99200     -0.18919      1    O
 7.19917
     3.99200      5.98800     -0.18919      1    O
 7.19917
    -5.98800      3.99200     -0.18919      1    O
 7.19917
     3.99200     -5.98800     -0.18919      1    O
 7.19917
    -5.98800     -3.99200     -0.18919      1    O
 7.19917
     0.00000      5.98800     -4.22319      1    O
 7.32745
     0.00000     -5.98800     -4.22319      1    O
 7.32745
     5.98800      0.00000     -4.22319      1    O
 7.32745
    -5.98800      0.00000     -4.22319      1    O
 7.32745
     0.00000      3.99200     -6.29667      1    O
 7.45548
    -3.99200      0.00000     -6.29667      1    O
 7.45548
     3.99200      0.00000     -6.29667      1    O
 7.45548
     0.00000     -3.99200     -6.29667      1    O
 7.45548
     7.98400      0.00000      0.00000      3    Ti
 7.98400
     0.00000     -7.98400      0.00000      3    Ti
 7.98400
    -7.98400      0.00000      0.00000      3    Ti
 7.98400
     0.00000      7.98400      0.00000      3    Ti
 7.98400
 END
```

CURRICULUM VITAE

Name　　　　　　Phanupong Phaktapha

Date of Birth　　27 January 1990

Place of Birth　　Roi-et, Thailand

Nationality　　　Thai

Education

2008-2012　　　　Khonkaen University,Khonkaen,Thailand

　　　　　　　　Bachelor of Science (Physics)

2012-present　　　Currently enrolling in Master's degree majoring in

　　　　　　　　Applied Physics, School of Physics, Institute of

　　　　　　　　Science, Suranaree University of Technology, Nakhon

　　　　　　　　Ratchasima, Thailand